![CEA logo]

COMMISSARIAT À L'ÉNERGIE ATOMIQUE

DSM - DAPNIA

DIRECTION DES SCIENCES DE LA MATIÈRE

DEPARTEMENT D'ASTROPHYSIQUE, DE PHYSIQUE DES PARTICULES,
DE PHYSIQUE NUCLÉAIRE ET DE L'INSTRUMENTATION ASSOCIÉE

SACM

SERVICE DES ACCELERATEURS DE CRYOGÉNIE ET DE MAGNÉTISME

CEA-DSM-DAPNIA-SACM
contribution to the IFMIF transition phase
2003

1 Introduction and Background

The International Fusion Materials Irradiation Facility (IFMIF) requires generation, by a linear accelerator (linac), of 250 mA continuous current of deuterons at a nominal energy of 40 MeV, with provision for operation at 30 MeV and 35 MeV. The basic approach is to provide two linacs modules, each delivering 125 mA to a common target. This approach presents availability and operational flexibility advantages.

The accelerators begin with a deuteron ion source and a low-energy beam transport to a radiofrequency quadrupole (RFQ), buncher and preaccelerator up to ~5 MeV. A high-energy beam transport from the accelerator to the lithium target must perform a variety of functions, complicated by the presence of strong space-charge forces within the beam. A very low beam loss along the accelerator and transport lines is required in order that maintenance can be performed without requiring remote manipulators.

The Transition year was initiated in 2003 with the objective of continuing the "Key Element Technology Phase" (KEP). The activities defined here concentrate on key engineering development items of the Accelerator Facility system. Consequently, the task can be structured into

Source (deliverable 1). Experimental demonstration of D and H_2^+ ions extraction improvement, maximum performance and reliability of the system; optimization of H_2^+ production for conditioning and facility testing; diagnostics development.

RFQ and DTL accelerator (deliverable 3), analysis of possible alternatives developed in KEP phase, to the reference design of accelerator system.

RFQ and DTL accelerator, HEBT (deliverable 5): engineering design outline, establishment updated reference design outline with focus on RFQ, DTL, matching section and high energy beam transport (HEBT).

The IFMIF work is carried out at the CEA in the framework of a considerably larger activity presently undergoing in the field of high-intensity linear accelerators [1,2]. The activity specific to IFMIF has been concentrated on:

Deliverable 1a: Development of critical accelerator components: ECR source/LEBT system.

Deliverable 1b: Development of diagnostics for high power CW.

Deliverable 3: Improvements and alternatives to the reference design.

Deliverable 5: Engineering and HEBT.

We report here the results obtained accordingly with the task. The major preceding report was :

CEA-DSM-DAPNIA-SACM contribution to the IFMIF KEP phase June 2000 to December 2002, Ref DSM/DAPNIA 03-72 [3]

2 Source development (TW3 TTMI 001 – D1)

2.1 Source reliability test

Beam characteristics and source behavior have to be recorded and compared with a reduce beam current in order to have a better understanding of the availability process. This describes the so called "over-design" process. Statistics of the over-designed principle was conducted with a lower beam current (30mA, see Figure 1) and compared to the 120 mA statistics. To obtain low intensity beam the source was set with a 4.8 mm diameter extraction aperture. With this plasma electrode, the plasma density remains quite constant and the species fraction do not change.
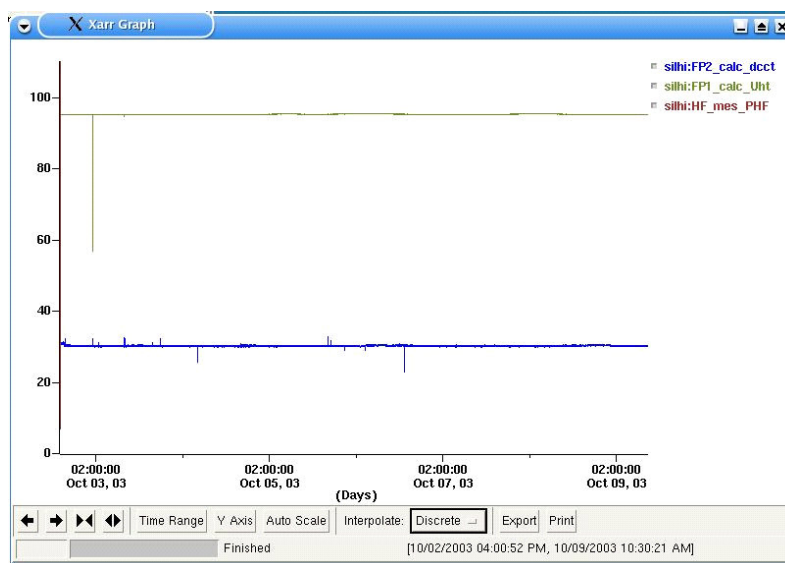
Figure 1 : 162 hour reliability test with a 30 mA – 95 keV CW proton beam.

Figure 1 presents the recorded high voltage SILHI platform potential (95 kV) in green. This curve shows an important failure due to a spark occurred about 10 hours after the beginning of the run. In fact, only one recorded point (sampling time 2 s) is not measured at 95 kV. This spark did not lead to a beam interruption.

The blue curve shows the extracted beam current. At 30 mA, some instability was observed, but no beam interruption over the sampling time was observed.

Previous high intensity reliability tests demonstrated source availability always higher than 95 %. Two runs of more than 100 hour showed higher than 99.8 % reliability. A new one-week test (162 hours) with a 110 mA – 95 keV beam has been performed. As previously observed, an average of 3 or 4 plasma extinctions led to 2.5 min beam interruption each day. The MTTR was 2.5 min and the maximum time between failures was 28 hours. The achieved availability reached 99.3 %.

2.2 Neutron production in the LEBT

Low intensity deuteron beam has been produced for neutron emission measurements. The source was equipped with a small diameter (4.8 mm) extraction system to limit the intensity. A 5 mA – 40 keV CW Deuteron beam was produced. The neutrons were measured online with a LB 6411 probe.

We were under a permanent control of the radiation safety service for this neutron measurement test. This experiment allowed acquiring data on 2.45 MeV neutron emission from (d,D) reaction.

After a short period in pulsed mode (10 ms/s and 120 ms/s) to evaluate the phenomenon, the beam was rapidly produced in CW mode. Finally the source worked in deuteron for 4 days. The neutron probe equipped with was located at about 40 cm from the beam stop (outside the beam line, behind a 25 mm thick stainless steel flange). A maximum neutron production saturated dose of 420 µSv was observed. The preliminary conclusions of the measurements are as follow:

- The neutron emission appears isotropic around the copper target and follows the $1/d^2$ decay rule.
- After the start of the beam, the neutron emission rise time is rather short and reaches a saturation level.
- The saturation level linearly depends on the intensity of the beam.
- The neutron emission rise time depends on deuteron energy and beam intensity.
- The neutron emission rise time is about 1 hour with a 5 mA-40 keV deuteron beam on cleaned target and shorter after a beam restart on deuterium polluted target.
- The neutron emission fall time is very short when the beam stops (from 415 to 25 µSv.h^{-1} after 6 min and 0.5 µSv.h^{-1} after 30 min).

Figure 3 presents the total source extracted beam (between 7 and 7.3 mA) measured at the exit of the source to obtain 5 mA on the copper target. Figure 4 presents the neutron emission acquired by the LB 6411 probe. These measurements have been performed over a 6 hour long run with no beam off. On Figure 4, the red curve shows the neutron emission fall time just after the beam stops.

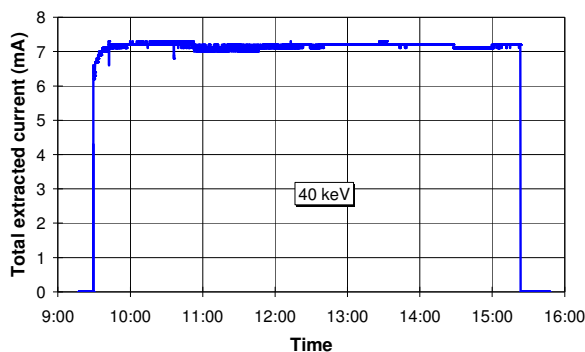Figure 2 : picture of the probe installation on the beam line.

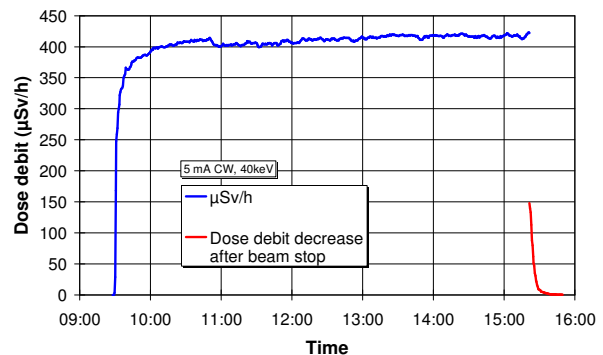Figure 3 : total extracted current for the neutron production measurement.

Figure 4 : Measured dose debit with deuteron (blue) and decrease after beam stop (red)

2.3 IFMIF H_2^+ measurements with the SILHI ECR source

2.3.1 Introduction

In the framework of the IFMIF studies, measurements were undertaken at the CEA/Saclay laboratory. Those experiments, realized with the SILHI ECR source installation, aimed at the maximum production of molecular ions (H_2^+) while injecting hydrogen gas in the plasma chamber. IFMIF is foreseen to accelerate deuteron beams (2x125 mA) at 40 MeV for material behavior investigation. The H_2^+ ions acceleration would help the commissioning of such a high intensity deuteron facility, especially by limiting neutron production before the industrial running mode.

The source has been designed and developed to maximize the atomic ions H^+ or D^+ intensity. Routinely the atomic ion fraction is higher than 80 % by adjusting the parameters with an optimized set up. For example, to increase the plasma density, boron nitride discs are simultaneously installed at both ends of the plasma chamber. As the source would have to produce, either a high D^+ fraction or a high H_2^+ fraction (depending on the injected gas in the plasma chamber), it is unthinkable to modify the source geometry (to change the plasma electrode, to remove the BN discs or other…). So the following possible actions were

(i)   Tuning of the magnetic configuration,

(ii)   Modify the injected RF power and/or H_2 gas pressure,

(iii)   Mix some gases (Ar, Xe, Ne, N_2, H_2O, CO_2 for example).

The results of the different measurements are reported in section 2.3.1.2, while the first section (§2.3.1.1) briefly summarizes the SILHI characteristics and the diagnostics set up.

2.3.1.1 I - Source and diagnostics devices

The SILHI ECR source is operating at 2.45 GHz. The RF power is fed into the plasma chamber from a 1.2 kW magnetron via a 3-step ridged transition, a quartz window and standard WR 284 rectangular waveguides. Two independently tunable coils provide the magnetic field. The beam is extracted from the plasma though a single aperture pentode extraction system. To determine the beam energy, the source is biased by a HV power supply (up to 100 kV). A 3 insulator accelerator column (27 cm long) allows an under vacuum continuity from the source to the low energy beam transport. Two 1000 l/s turbomolecular pumps are used to empty the beam line where several diagnostics allow beam characterization.

The Wien filter designed for the emittance measurement unit (EMU) allows the high intensity beam species analysis (Figure 6). A Tantalum sampler (0.2 mm diameter) is inserted in the middle of a 40 mm thick Copper bloc (15×15 cm) to select a beamlet. Then the selected particles cross a permanent magnet dipole (now made of 6 SmCo magnets, see §2.3.1.3) coupled with a ramping electric field (up to 1 MV/m) provided by 2 symmetrical electrodes. Finally, the current collected on a thin wire (equipped with secondary electron suppressor) allows measuring the different species fractions.
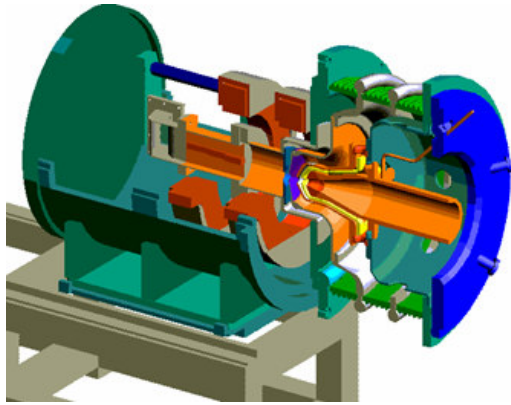
Figure 5 : Source 3D drawing.   Figure 6 : Emittance Measurement Unit
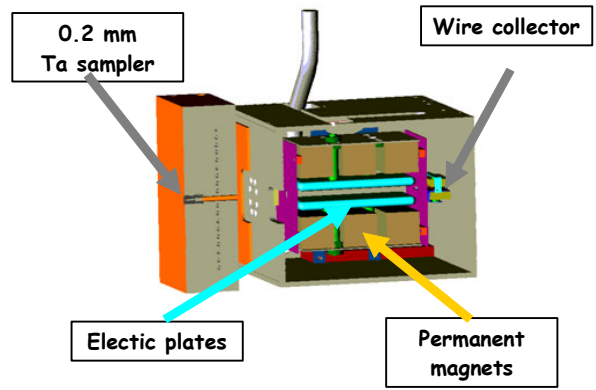
The EMU is located at the exit of the accelerator column (53 cm from the extraction aperture). Home made Labview interface allows the EMU displacement by steps as low as 6 µm (usually set around 0.1 mm to 1 mm) across the beam diameter. When the sampler hole is located on the beam axis, the species fraction is measured. The collected beamlet current, read as a function of the electric field is acquired and automatic routines calculate the species fractions. The results shown on Figure 7 are considered as classical species fraction in daily running mode.
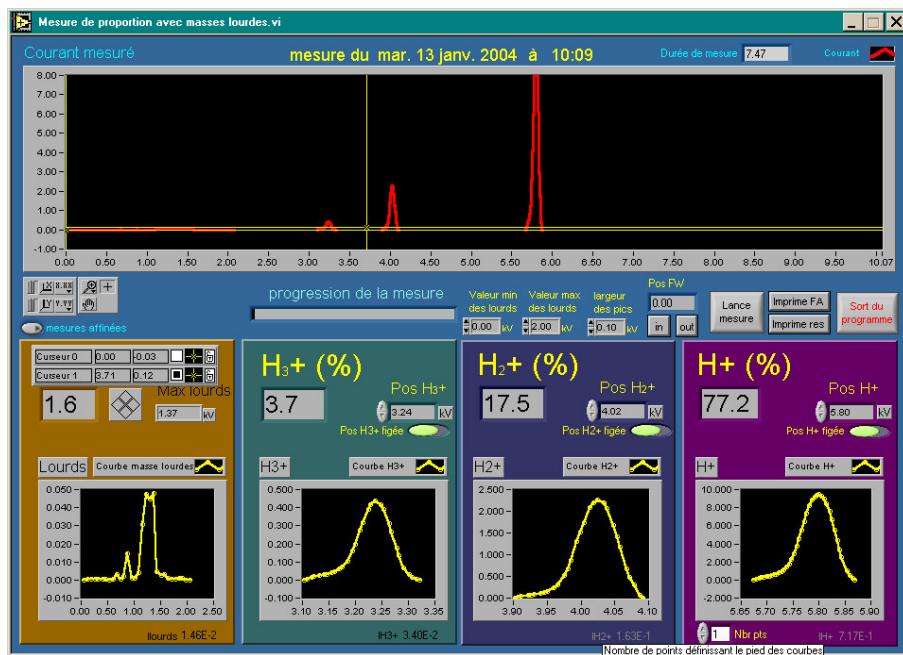
Figure 7 : Measured atomic atoms fraction.

2.3.1.2 H_2^+ optimisation experimental results

First measurements have been performed by tuning the magnetic configuration. For each source set of parameters, the species fraction and the extracted intensity are recorded (see table 1 and Figure 8). One could note, as previously observed, that the H_2^+ fraction increases while the extracted beam intensity (relevant from the plasma density) decreases. These measurements also indicate it does not depend on the magnetic configuration; it continuously ranges from 15 to 21 %, with the different magnetic set up while the current goes down from 100 to 78 mA.
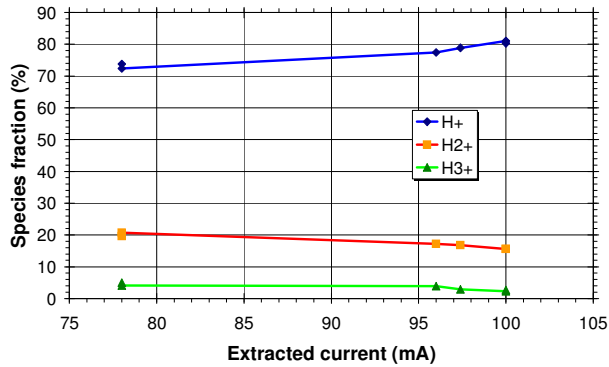
Table 1 : Measured results.

B1	B2	I (mA)	H$^+$	H$_2^+$	H$_3^+$
41.4	94	100	80.3	15.6	2.7
30	100	100	81	15.6	2.3
35.7	100	97.4	78.9	16.8	2.9
100	65	96	77.4	17.2	3.9
35	90	78	72.4	20.7	4.1
41.4	94	78	73.8	19.6	5

Figure 8: Species fraction versus extracted beam
current

Other measurements, achieved by changing the injected hydrogen gas flow, led to a variation of the pressure into the plasma chamber (see Figure 9). In fact, due to the short remaining time, experiments have been done with a 70 mA – 73 kV beam to avoid to melt the new Ta sampler. With hydrogen flow lower than 2.5 sccm, the RF power has been dramatically increased to maintain an almost constant extracted current (70 mA total). In spite of everything, in these conditions the extracted beam becomes instable.

Figure 9 : Species fraction versus hydrogen gas injection.

To stabilize the beam, several mixing gas injections have been tested with no significant improvement on the molecular ion intensities. The main effect is the presence of important heavy ion fraction (up to 25 % with 0.4 sccm of neon for example) shown on Figure 10, on the left window.
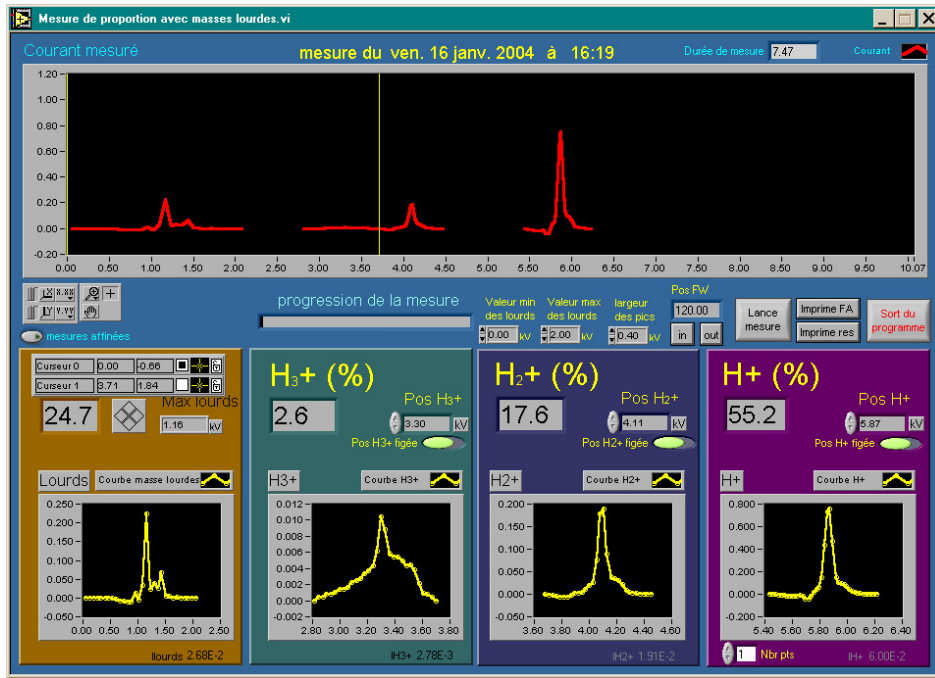
Figure 10 : Best H_2^+ fraction.

2.3.1.3 Gas mixing

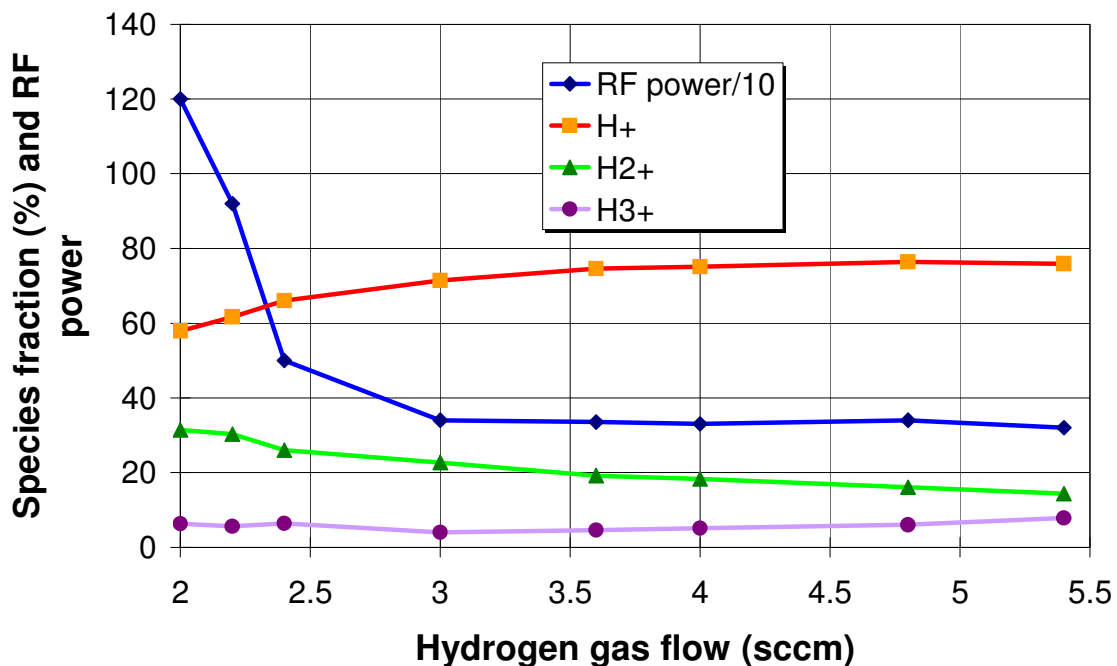In 2001, previous measurements done while a hydrocarbide pollution affected the source, indicated an important H^+ fraction degradation (down to 40%). For this reason, specific measurements have been performed by injected controlled gas in the plasma chamber. We tested successively Ar, Ne, N_2, H_2O and CO_2. This does not allow to significantly increase the H_2^+ intensity.

For this, the source was tuned in routine mode (100 mA-95 kV). A second gas flow controller, installed in parallel with the permanent one allowed injecting additional gas directly into the plasma chamber. Rapid measurements have been performed with nitrogen or argon. This did not show any significant increase of the H_2^+ intensity. We also tried to keep the global pressure constant (by decreasing hydrogen injection while injecting additional gas) with the same results. The neon gas experiment is reported in §2.3.1.2, Figure 10 and the text above.

Figure 11 : Comparison of the species fraction with (red) and without (blue) water injection

Moreover, tests have been achieved with additional water gas into the plasma chamber. Previous experiments performed in Los Alamos Laboratory indicated an increase of H_2^+ ions with the addition of a very small amount of water. Here, the experiment has been achieved with a 100 mA at 95 keV. Figure 11 compares the species fraction with and without water inje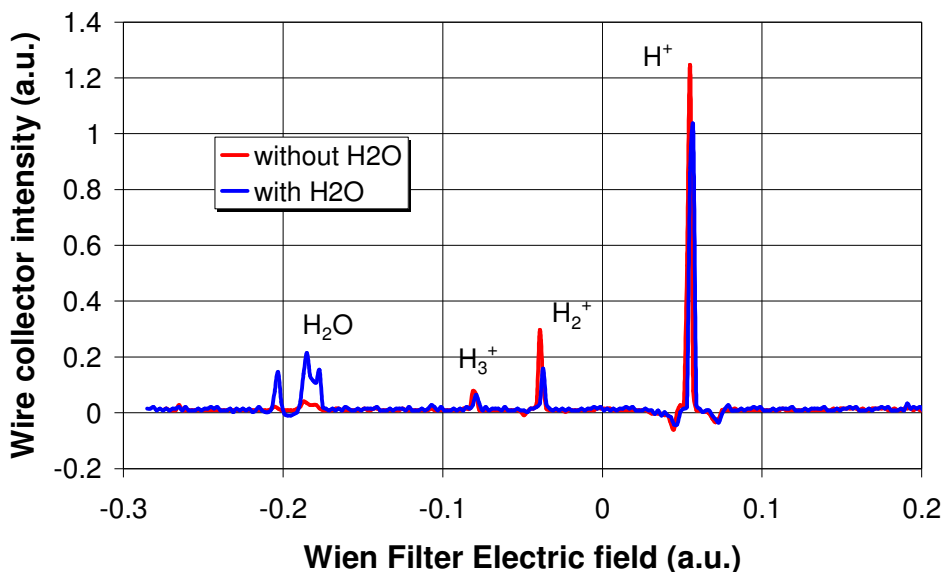ction. With 0.22 sccm water injection, the beam line (LBE) pressure rose from $1.79\ 10^{-5}$ to $2.2\ 10^{-5}$. The results indicate the heavy ions peak grows while H^+, H_2^+, H^+ peaks decrease.

A second series of measurements have been performed after sampler change (due to Tantalum melting) with a lower power beam. With a very small amount of CO_2 gas, the species fractions vary as reported in the following table:

Table 2 : CO_2 additions

	Pure H_2	With CO_2	With CO_2
Energy (keV)	78	78	78
Beam intensity (mA)	70	52.9	53.9
CO_2 Gas flow (sccm)	0	0.05	0.15
LEBT pressure (Torr)	$1.34\ 10^{-5}$	$1.5\ 10^{-5}$	$1.6\ 10^{-5}$
H^+ (%)	71	46.3	45.6
H_2^+ (%)	23	23.5	20.7
H_3^+ (%)	4	10.5	8.8
Heavy ions (%)	1.9	19.7	25

This table clearly shows an important degradation of the beam characterized by a dramatically drop of the intensity and an important increase of the heavy ion fraction. The stability of the source was also affected. This occurs with the injection of a very small CO_2 amount. As a result, the H_2^+ *fraction* does not change (relatively) but finally the total amount of H_2^+ ions decreases.

To conclude, oil pollution degrades significantly, and in an almost permanent way, the source behavior. As a result, the H_2^+ molecular ion fraction increases but it is not a controllable mode. For this reason we were not willing to test this possibility, and we do not recommend this solution.

2.3.1.4 Encountered problems with permanent magnets.

The Wien filter was previously equipped with NdFeB magnets which reacted with the hydrogen gas. At the beginning of 2003, the magnet was destroyed and a long delay occurred to repair this device. This explains the delayed measurements.

Figure 12 : Picture of the exploded permanent magnet.

2.3.1.5 Conclusion

The above reported results do not show any important H_2^+ ion fraction improvement by changing the source parameters. So to conclude, one can expect a maximum H_2^+ current equal to 30 mA with a total 150 mA extracted beam. This means some adaptation in the LEBT, in order to avoid degradation of equipment with such a high power deposition in the line. Of course no

measurements compare D^+ and H_2^+ emittances during this campaign and we cannot ensure such a molecular beam could be sufficient for the IFMIF accelerator commissioning.

One may think of other commissioning possibilities, like debugging the accelerator with H^+ current (in order to verify the right quadrupole focalisation, for instance), and to quickly switch to D^+ beam, with a low current and a low duty cycle. The different options will have to be discussed among the accelerator team.

The design of a dedicated source for H_2^+ production is therefore highly recommended if IFMIF maintains the need of H_2^+.

2.4 Beam diagnostics.

The development of diagnostics continues. It is mainly attached to the Doppler shifted profile measurement, useful as a non interceptive measurement, and the wire scanner. Some drawings are already made, and the scanner wire was tested with success, in pulsed mode since it is an interceptive diagnostics. The beam energy deposition prohibits CW wire scanner analysis.

Figure 13 : picture of the scanner wire
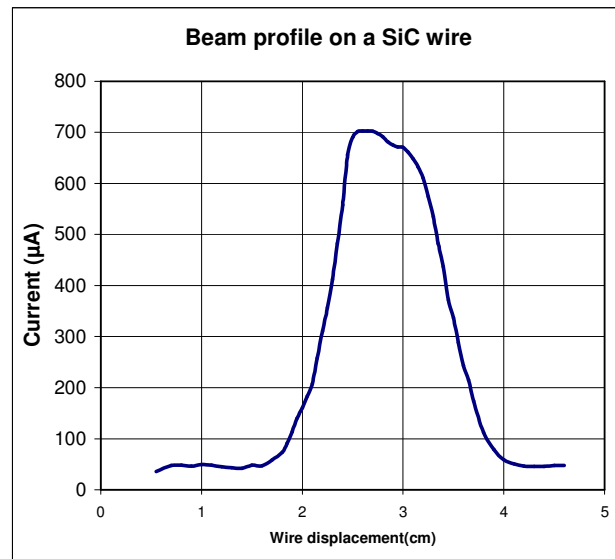
Figure 14: Measured beam profile on a 85 mA – 95 keV beam
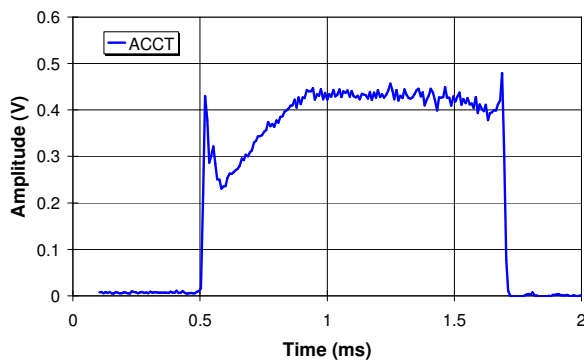
Figure 15 : ACCT measurement of the beam pulse
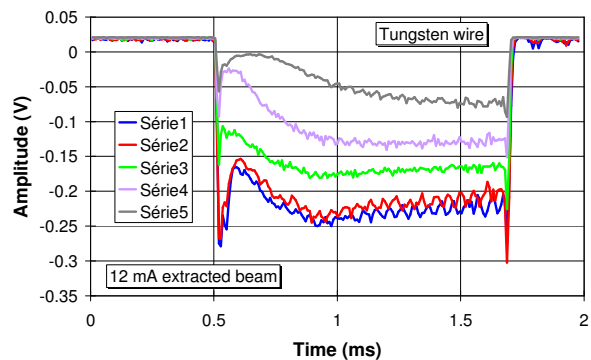
Figure 16 : Wire scanner time dependence to be compared with the preceding figure.

The mechanical resistance of the wire was tested, the electronic was validated, and the profile was acquired (Figure 14). The time dependence of the response is comparable to the current transformer diagnostics (see Figure 15 and Figure 16). The Silicium carbide wire shows a very good resistance to deterioration and allows the observation of a 2 ms 95 mA 95 keV pulse at 1 Hz repetition rate.

3 Alternatives of the design (TW3 TTMI 001 – D3)

3.1 Cavity types

One of our actions was to identify the different RFQ types available. We were helped in this task by Romuald Duperrier who made such a comparison for the RIA project at MSU [4]. This project is at 80 MHz, about 2 times a lower frequency than the IFMIF project. Nevertheless the results are fully relevant for the IFMIF RFQ. One has to remember that 80 MHz is much easier to build from the engineering point of view.

A comparison of the power consumption of the most common RFQ structures was made: split coaxial, four rods, IH, and four vanes. The quality factor and peak power densities were computed and compared whenever possible with some experimental case (3D extremity of the IPHI RFQ).
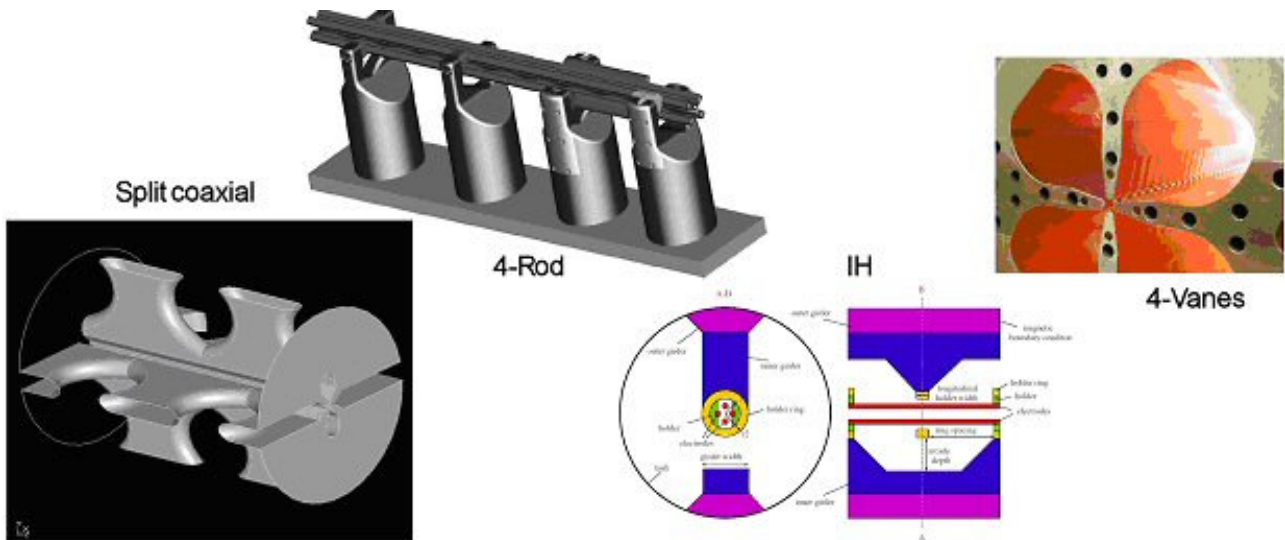
Figure 17 : The cavity types evaluated for the comparison.

In all the above RFQ cases the hypotheses were kept constant (same aperture, same vane voltage, same frequency). It is exactly the same accelerating structure.

3.1.1 Split coaxial

The split coaxial is a kind of 4-vanes RFQ with coupling cell between the vanes. It is a low power consuming cavity type. This property allows high voltage and big apertures (1 cm) especially at low frequencies and might be relevant for heavy ions when four vanes RFQ could be estimated too bulky. The main advantages of conventional Split Coaxial RFQ resonators are :
- High shunt impedance
- Good tuning possibilities
- No dipolar component
- High mechanical stability

In Table.3, below, the structure was not completely optimized. Usually, we try to minimize the transverse size by using this type of cavity. Doing so, the coupling windows increase in size and the power dissipation (and peak power) increases. Nevertheless, the order of magnitude is more than sufficient to take a decision.

3.1.2 Four-rod

Four rods RFQ accelerators are well established and are the most common structure for the acceleration of heavy ions, generally in pulse mode. This 4-Rod RFQ was optimized by Holger J. Podlech for the same RIA project [5]. Among the advantages of 4-Rod RFQs, one can quote:

- Low cost
- Suitable for heavy ions accelerator
- Strong European team
- Small transverse size

3.1.3 IH RFQ

The IH was again optimized by Holger J. Podlech for the RIA project [5]. IH RFQs are relatively new developments. The first IH RFQ has been commissioned successfully in 1999 at GSI. The resonant structure consists of two girders carrying the support rings and mini-vane like electrodes (see Figure 17). Due to the small distance between the support rings (~10 cm), the losses around the electrodes are very small compared to four rods RFQ. This reduces the cooling requirements in this area. The main advantages of IH RFQ resonators are :

- Good shunt impedance and excellent distribution of losses
- Good tuning possibilities
- High field symmetry
- High mechanical stability

3.1.4 Four-vane

The 4-Vane structure is the eldest one and the most built for RFQs. It has been used for CW operation at 80 MHz [6] and at 350 MHz successfully [7,8]. It is the reference design. 4-vanes RFQs are well known in the laboratory [9]. They have shown good reliability in CW condition [10]. The main disadvantage is that the inductance is only 2D. This induces huge transverse cavities at low frequency. Due to the perfect quadrupolar symmetry, no dipolar component is present in the four vanes cavity. It is the most stable cavity type among the 4 presented, and allows the best field tuning.

In order to show a fair comparison, the following table also shows the 3D extremity of this essentially 2D accelerator (where the peak power loss is located).

3.1.5 Results.

Table.3 : Comparison between RFQ structures

	Split Coaxial	Four rods	IH	Four vanes
Q	13985	6311	9362	17901/12819
E_0 (MV/M)	17.73	20.00	19.34	17.41
B_0 (T)	0.0048	0.0340	0.0126	0.0074
Power loss (kW)	49.2	80.4	77.8	37.46
Peak power loss (W/cm²)	1.75	91.48	10.71	4.34

This table generates a few comments :

- Four vanes structures are the less consuming structures (more than a factor 2 compared to 4-rods or IH)

- Four rods RFQs show a very high peak power loss. The value can be manageable (we deal with higher peak value in the IPHI RFQ), but induces engineering difficulties and possible deformation in CW mode. This promises to be even more problematic at the IFMIF frequency of 176 MHz.
- Split coaxial RFQs looks not far from 4-vanes RFQs.

Taking these results into account, we do not recommend to change from the 4-vane RFQ type.

3.2 Revisions and verification of the RFQ beam dynamics design.

We looked at the different RFQ design of the IFMIF RFQ. The comparison extended to various RFQ codes, with the help of Dr. R. Jameson that we thank here. The first RFQ design was made in June 2002 by CEA-Saclay, and is documented in the previous report [3]. The second one was provided during the same period by the Frankfurt team. Both designs showed a length of about 12.5m, and cannot be compared on that point.

Table 4 : comparison of the 2 RFQ dessign

	Saclay	FZK
Length (m)	12.482	12.211
Kilpatrick	1.76 at cell 8	1.64 at cell 656
Max vane voltage (kV)	130	152
Min vane voltage (kV)	96.5	67
Mean voltage (kV)	102.7	100.7
TOUTATIS Transmission (%)	98.4	97.12

There was a question on the results of the different RFQ simulation codes. We already know from a previous analyses that [11]:

PARMTEQM is not good for particles coming too close to the vane, as it is usually the case with high intensity beam. Above the circle defined by the minimum vane aperture, the fields are not well describes (10% error on some surface, 100% error on some spots). Depending on the PARMTEQM version, the particles might be considered lost above the square defined by the minimum vane aperture. This may lead to more losses (around 4.4%) on some design. Some paraxiality was left in the PARMTEQM code, even when it was sure that it has been removed (found in the movement integration, Vtot=Vz). Some comparison was made between PARMTEQM with and without paraxiality and TOUTATIS, with the assumption that a particle is lost on a square (like in PARMTEQM). The following table showed the results obtained at that time [11]:

	Transmission
Toutatis with the square	92.45%
PARMTEQM with some paraxiality	87.22%
PARTEQM without paraxiality	92.48%

These results depend on the confinement level of each design and may vary, but the tendency is described.

Some precisions:

TOUTATIS can use a vane profile input file (name "xxx.vane") which describes both the longitudinal and the transverse shape of each four vanes (or rods). Since TOUTATIS calculates the 3D fields in real time, it can simulate all type of vanes defects, and naturally includes multipoles, images effects etc…

The space charge routine is a simplectic 3D routine.

3.2.1 Input of the codes

The assumptions in the simulations are:

- Input emittance = 0.25 π.mm.mrad rms normalised, 4D waterbag distribution leading to 1.5 π.mm.mrad total normalised emittance.

- Input current such that 125 mA are accelerated out of the RFQ. In CEA-Saclay design this leads to 130 mA, input beam.

- No coupling gaps, since the exact number of coupling gaps was not yet fixed at the time of the comparison

- Sinusoidal z profile, $\rho \neq$ const., $\rho/R_0 \neq$ const.

3.2.2 TOUTATIS results on the Saclay design:

- In real 3D field : **98.4%** of transmission

- With the 2-term formulation activated: 99.5% (image effects). The 2 terms option could not explain a lower transmission.

- With the 2-term options and the "lost on square" option : 95%

- At 0 current : 100 %

- The output transverse emittance is equal to 0.28 π.mm.mrad.

3.2.3 TOUTATIS results on the Frankfurt design:

With 0.25 π.mm.mrad *rms* normalised input emittance and 130mA, the transmission is **97.12%.** The output transverse emittance is equal to 0.28 π.mm.mrad

3.2.4 Dr. Jameson version of PARMTEQM on the Saclay design:

- 91.1% transmission, lots of effort since TOUTATIS is not generating the B and A column value.

- 100% at 0 current.

3.2.5 PARMTEQM

- With multipoles, square criteria and some paraxiality : 83% transmission

- Corrected version, with multipoles and square criteria : 90%

3.2.6 LIDOS.RFQ simulation.

The Saclay design was tested with the LIDOS.RFQ code. We spent a lot of time to ensure that we where simulating the same 3D copper profile of the vane. Then, LIDOS.RFQ has a different way

to calculate the 3D field and the transport (compared to TOUTATIS), but there is again much less approximation in both TOUTATIS and LIDOS compared to analytical codes. The input beam was a 4D WB distribution. The transmission was 98% with 97.8% of accelerated beam.

3.2.7 Conclusions:

The 2 terms formulation run in TOUTATIS shows that we may have confidence in the external field calculations of the TOUTATIS code. PARMTEQM is pessimistic for beam simulations which are big compared to the aperture.

There is not much difference between the two RFQ design. The Saclay design shows a slightly higher transmission, and a lower peak vane voltage, but both arguments are weak.

We kept the CEA-Saclay design in our simulations described below (§6) especially for the error study.

3.3 Reflections on the RFQ 2D cavity

The optimization was greatly simplified with the use of the 2D code SUPERFISH. Compared to other 3D codes, results are extremely fast and reliable to obtain.

The objectives described in this section were to test some tricks able to reduce the transverse size of the RFQ. A smaller transverse size means less expensive copper and a lower machining process. This analyses was made previously to the 2D shape optimization described later in this document (see §4 below). For this only reason some discrepancy appears in the 2D shape. Nevertheless the tendency is accurately calculated and do not change the conclusion.
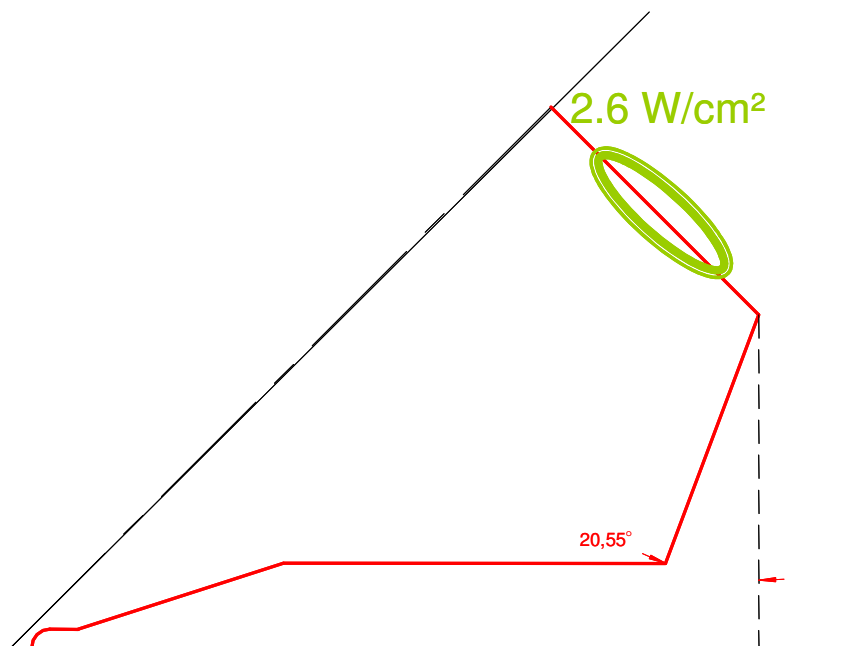

2.6 W/cm²

20,55°

Figure 18 : 1/8 of RFQ

Figure 18 above shows the 2D cross section used for this analysis. SUPERFISH calculations showed that the peak power loss, in 2D, is expected to be located in the bottom of the RFQ (see Figure 18). The SUPERFISH power consumption was found to be equal to 61 kW/m with only 90 kV on the vanes.

A tentative was made to compensate the magnetic length of the RFQ (the bottom cavity, where is located the peak power loss), with an increased capacity around the beam axes. As it is not allowed to modify the vane tips profile, the idea was to introduce an over-thickness that we name the crocodile effect (see Figure 19).
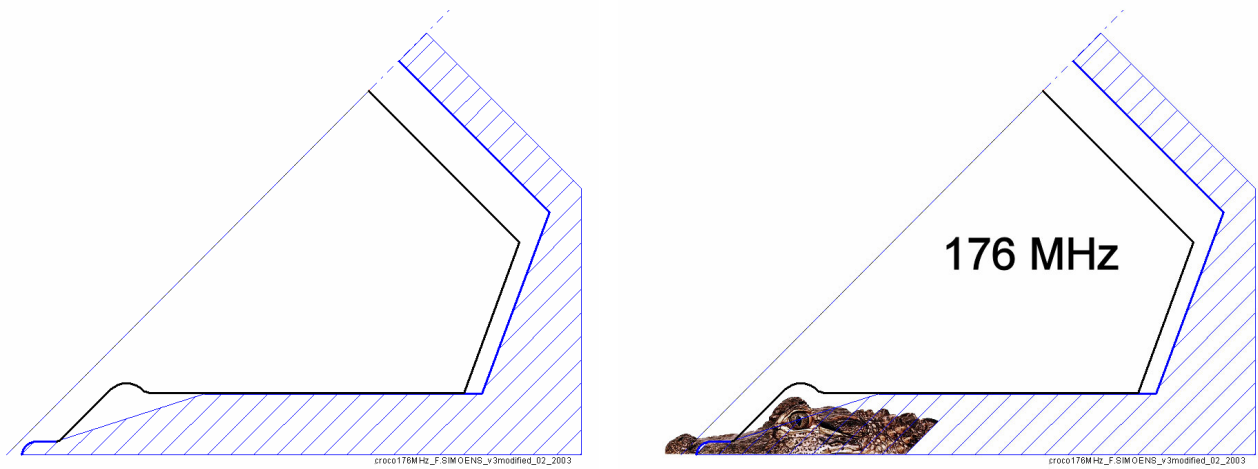

Figure 19 : The crocodile effect

The transverse dimension was easily reduced by 8%, but this was at the cost of a much higher hot spot and power consumption. The peak power loss increases by 41% and the total power by 35%.

Knowing that the power consumption is already a difficult point of the project, since it leads to use more of the expensive diacrode, we abandoned this idea.

4 RFQ 2D cross-section design (TW3 TTMI 001 – D5)

4.1 Introduction

The cross-section of IFMIF RFQ cells is inspired from that for IPHI RFQ : each quadrant is wholly described by the few geometrical parameters illustrated on Figure 20. On this figure, green parameters are given by beam dynamics optimizations, red ones remain constant along the RFQ, blue ones are fitted to quadrupole mode resonant frequency. As an example, for IPHI, $x_M = y_M = 71.2$ mm, $h = 7.4$ mm, $j = 56.5$ mm, $\alpha = 10°$, $r = 20$mm.
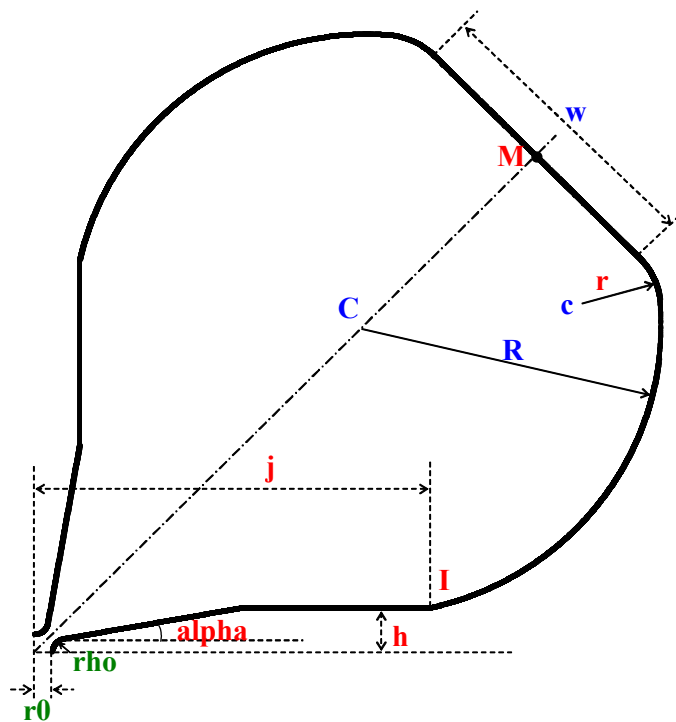

Figure 20: geometrical parameters describing IPHI and IFMIF RFQ cell cross-sections

IFMIF RFQ quadrupole mode resonant frequency has to be 175 MHz which is roughly IPHI half-frequency. An easy way of doing would be to simply double the main sizes. Instead, an attempt was made to still decrease the power losses. Moreover, it was chosen to make the flat bottom wide enough to allow the insertion of appropriate slug tuners and vacuum port anywhere along the RFQ. The process used is described in the following paragraphs. §4.2 explains which geometrical parameters were chosen to remain constant along the RFQ and how they were determined from the detailed study of cell n°151. §4.3 displays the way of getting the right cross-sections for all the 586 cells and the corresponding power dissipation.

4.2 Optimization of the constant geometrical parameters

As shown on Figure 21, cell n°151 is one of those that have the smallest r_0 and ρ values and then should lead to the smallest w value for the accurate resonant frequency, compared with all the

other cells. A detailed study of that cell should permit to determine the main geometrical parameters that remain constant from cell to cell along the RFQ.

Among all the geometrical variables illustrated on Figure 20, only few are independent. Indeed, there are some links between them through the following observations :

- the arc of centre $c(x_c,y_c)$ and radius r has to be tangential to both the flat bottom and the arc of centre $C(x_C,y_C)$ and radius R
- the vane flat segment and the arc of centre $C(x_C,y_C)$ and radius R must intersect at the point $I(j,h)$
- The points $M(x_M,y_M)$ and $C(x_C,y_C)$ belong to the symmetry axis of the quadrant.
- r_0 and ρ values are given by beam dynamics optimizations (Figure 21).
- The volume defined must have 175 MHz quadrupole mode resonant frequency.

Moreover, it was decided to take the same vane angle $\alpha = 10°$ and radius r = 20 mm as for IPHI RFQ, assuming that the machining of the cells could be made with the same tool. On the other hand, in order to still decrease RF power losses, the vane thickness was reduced, i.e. h = 12.5 mm instead of 2 x 7.4 = 14.8 mm. Finally, it was intended to design the cell n°151 with a flat bottom width w ~ 80 mm.
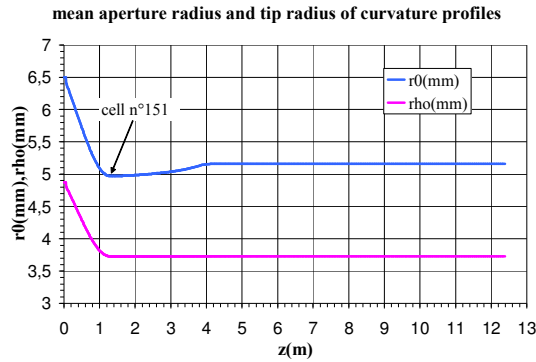

Figure 21 : Vane mean aperture radius and tip radius of curvature along the IFMIF RFQ
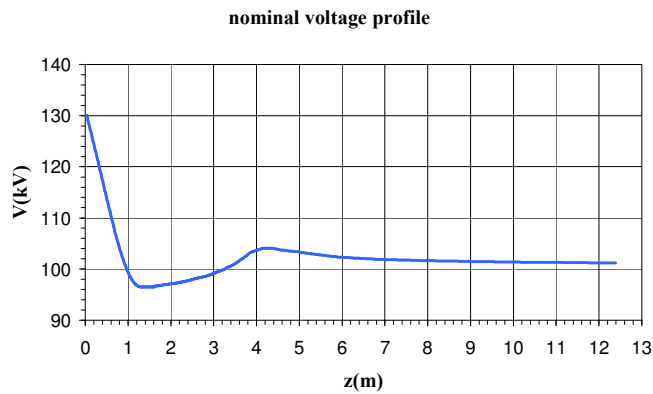

Figure 22 : nominal voltage profile

So, SUPERFISH program was run with different x_M and j values around twice those for IPHI, looking for optima as regards power consumption and flat bottom width.

Finally, the optimum geometrical parameters constant along the RFQ were found to be, for h = 12.5 mm, $\alpha = 10°$, and r = 20 mm : $x_M = 139$ mm and j = 110 mm. These values led to w = 80.34 mm with a resonant frequency of 175 MHz ± 1 kHz for cell n°151.

4.3 Optimization of all cross-sections

At that stage of the study, all the requisite data were available to compute the w values everywhere in the RFQ, the knowledge of c, C and R resulting from that of w. A special program interacting with SUPERFISH was written to fit the value of w to the accurate resonant frequency taking into account the same constraints as described above for cell n°151. The corresponding flat bottom width variations along the RFQ are plotted on Figure 23 and the cross-sections for the 3 most typical cells are shown on Figure 24.
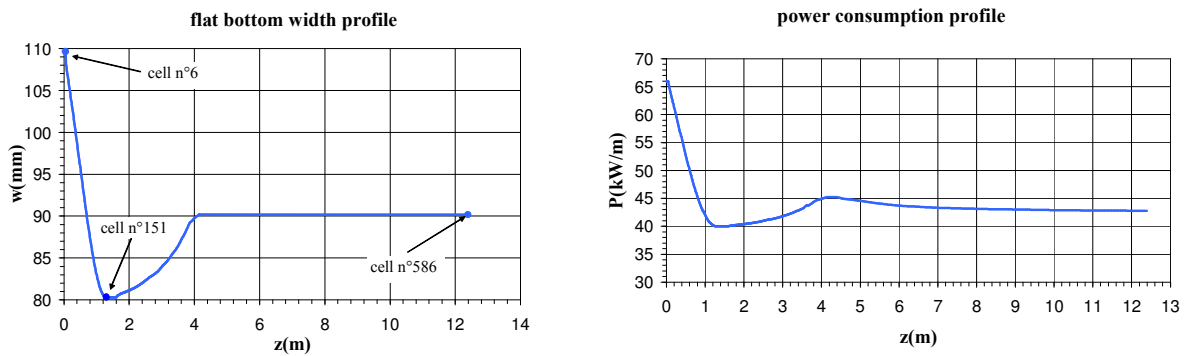

Figure 23 : Flat bottom width and power consumption variations along the RFQ.

Moreover, to perform the exact field calculations and thus return the exact power dissipation value, SUPERFISH program needs the correct normalization factor input : $E_0 = V/(2r_0)$. Of course, this factor varies from cell to cell. The fit program takes into account this evolution. E_0 is computed using both voltage and mean aperture radius corresponding points of the plots on Figure 21 and Figure 22. The 2D-power dissipation thus estimated is plotted on Figure 23.

The integration of the 2D-power dissipation along the RFQ then gave the optimized whole 2D-power consumption, on top of which 20% was added in order to take into account global 3D effects. This leads to P = 654 kW, about half of the power consumption expected. Adding globally 50% for the tuning, RF transport losses we obtain 981 kW. Adding the beam power (611 kW) we obtain a total of **1591 kW** allowing to envisage the use of only two RF systems instead of the three previously anticipated.
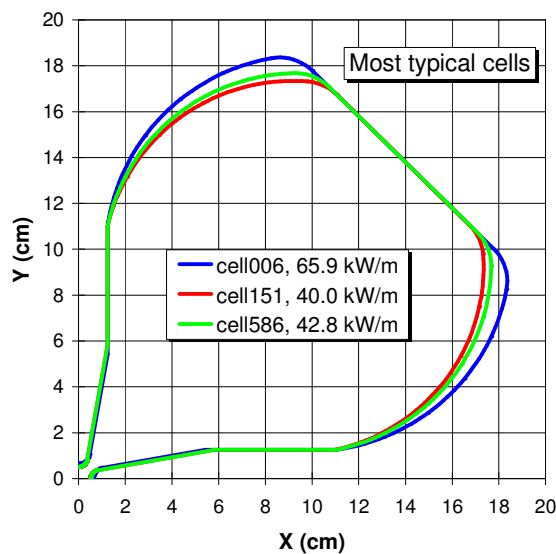

Figure 24 : Optimized cross-section for IFMIF RFQ most typical cells and corresponding power consumption.

4.4 4. Conclusion

The aim was to design the 2D cross-sections for all the 586 cells of the IFMIF RFQ in order that each cell has :

- 175 MHz quadrupole mode resonant frequency
- flat bottom wide enough to insert appropriate slug tuners and vacuum port.
- power consumption as low as possible.

This goal was reached.

Indeed, all the cells designed above have flat bottom width over 80 mm, with a resonant frequency of 175 MHz ± 1 kHz and with a whole power consumption of maximum 1591 kW which allows to save one rf system.

5 IFMIF RFQ Coupling gaps (TW3 TTMI 001 – D5)

5.1 Introduction

Resonant coupling segmented RFQ were first introduced by Lloyd Young from Los Alamos National Laboratory [7]. Resonant coupling in a segmented RFQ stabilizes the accelerating field against quadrupole-like perturbations. End rods are also used to stabilize the field against dipole-like perturbations. As a result, the distribution of nearby modes about the accelerating mode frequency is optimized.

Extensive analytical developments in Saclay now allow to calculate the effects of the segmentation on the RFQ quadrupolar component stability. We check the need of coupling segments and calculated the according gap width.

5.2 Normalized voltage error impulse functions

If we assume some capacitance perturbation in the space of distributions

$$\Delta C(z) = \frac{dC}{C(z_0)} \delta(z - z_0)$$

The resulting voltage error is $\Delta V(z, z_0)$, which is what we want to minimize.

We define the normalized voltage error impulse function as

$$\frac{\Delta V(z, z_0)}{V(z)} := h(z, z_0) \frac{dC}{C(z_0)}$$

Therefore we can compare RFQ designs with the norm defined as:

$$\|h\| := \sup_{z \in \Omega} \ \sup_{z_0 \in \Omega} \left| h(z, z_0) \right|$$

5.3 Results

5.3.1 Capacitance calculation

The resulting curves are given in Figure 25. The x axis is the value of the longitudinal capacitance in the segmentation. The y axis represents an estimation of the stability quality of the quadrupolar factor.

The pink curve represents the present IPHI design, and we may expect that the LEDA RFQ presented almost the same curve. The curve was calculated for an 6 m long RFQ with 3 resonant coupling segments. The dot green straight line represents the result of the IFMIF RFQ design without any resonant coupling segment, the cavity being a single whole cavity. The blue and brown curves represent respectively 2 and 3 segments. A minimum is observed for 3 segments, with a coupling capacitance of about 2 pf.

We recommend that the IFMIF RFQ be cut in three resonantly coupled segments. In such a case, the beam dynamics indicates that they will be located at 4.161 and 8.321 meter.
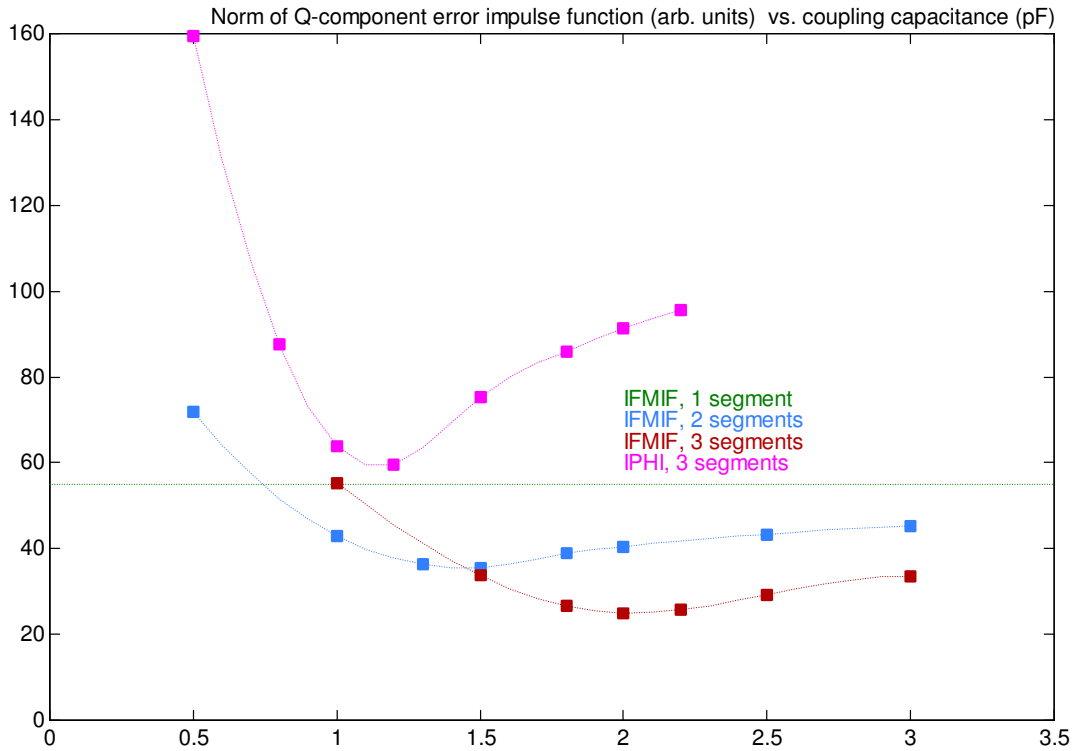

Figure 25 : Error impulse function versus coupling capacitance.

Another methods can be use to compute the gap capacitance. A. Pisent [12] calculates the gap capacitance as a function of the segment length and the linear quadrupolar capacitance:

$$C_{gap} = \left(\frac{\lambda}{2\pi} \right)^2 \frac{4C'}{L_{seg}},$$

with:

- Lseg the length of the segment,
- λ the wave length,
- C' the linear quadrupolar capacitance (pf/m)

In the IFMIF case, C' is constant as $\rho/R0$ is almost constant and its value is equal to 30 pf/m [13]. The linear capacitance is then the same as the IPHI RFQ. Using the above formula, if we want the same level of compensation with the segmentations, then the calculated gap capacitance is equal to 2.14 pf.

5.3.2 Gap calculation

The numerical calculation of the gap capacitance versus the gap properties was made with the Vector Field code TOSCA®.

Figure 26 gives the resulting curve. The gap width for a 2 pf capacitance is equal to 2.32 mm.
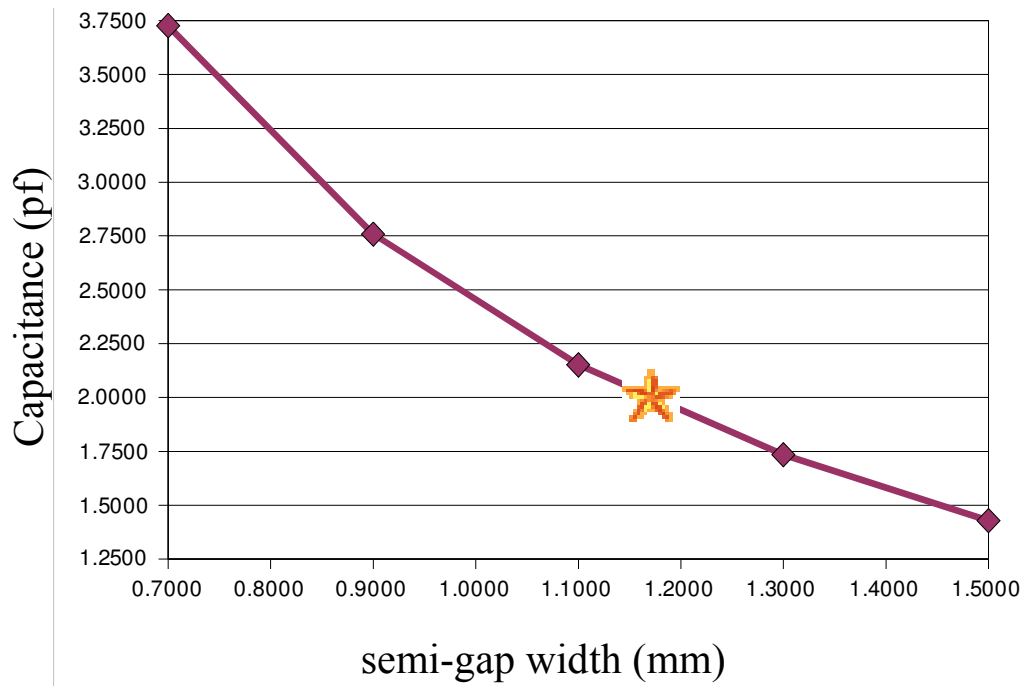
Figure 26 : evaluation of the gap width of the segmentation.

5.4 Conclusions

We found that we need 2 coupling gaps, 3 segments in order to minimize the quadrupolar error function in the RFQ. 1 segment would even work, but with less possibilities for the dipolar finger insertions.

Each coupling gaps is 2.32 mm wide.

6 The IFMIF High Energy Beam Transport line

(TW3 TTMI 001 – D5)

6.1 Introduction

The IFMIF project (International Fusion Materials Irradiation Facility) requests two linacs designed to accelerate 125 mA deuteron beams up to 40 MeV. The linac has to work in CW mode and uses a RFQ and 10 DTL tanks [3]. After extraction and transport, the deuteron beams with strong internal space charge forces have to be bunched, accelerated and transported to target for the production of high neutrons flux. This paper presents the HEBT line which provides a flat rectangular beam profile on the flowing lithium target and the beam dynamics end-to-end calculations include RFQ, DTL and HEBT with errors.
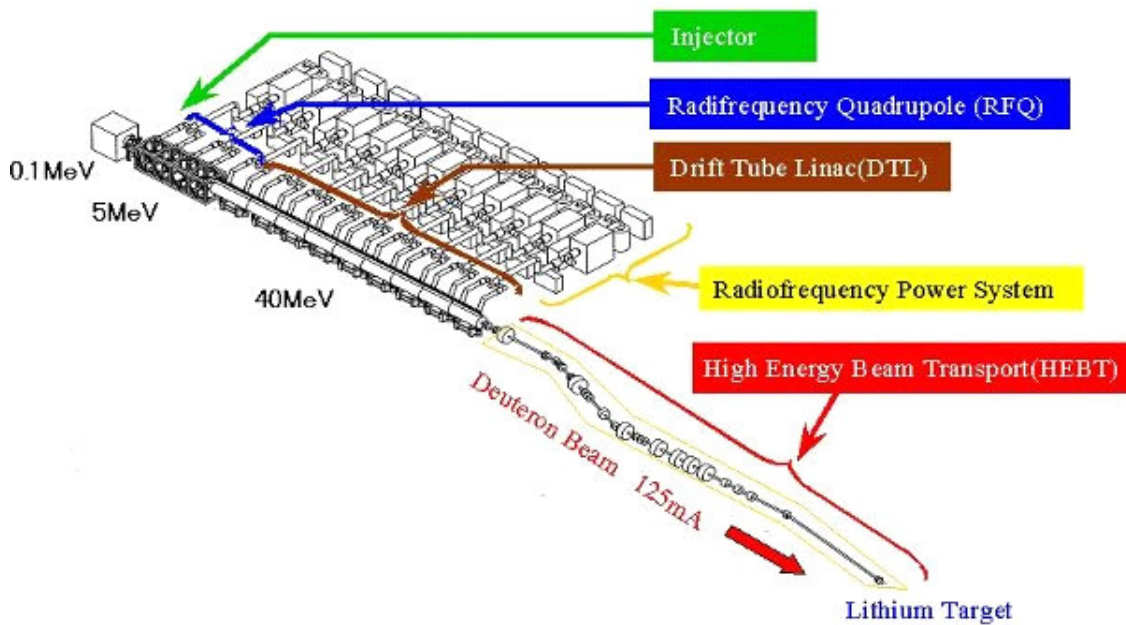
6.2 Requirements

Figure 27: General ifmif accelerator module layout.

The HEBT line has to transport the beam from the exit of the accelerator to the targets or the dump with the desired footprint sizes and characteristics. In normal operation, the footprint of each beam must be rectangular, 20 cm horizontal × 5 cm vertical at the flat top. The beam flux has to be approximately uniform (~5 %) across the flat top of the beam profile. The angle at which the beam intercepts the target result of a compromise between maximizing the flux in the test cell and minimizing the activation due to back streaming neutron. These two considerations indicate an optimum around 10°.

The horizontal separation between the target center and the axis of the linac, needed for concrete shielding, was estimate around 6.40 m by considering the A.E.S design [14].

6.3 General description

The incidence angle of each beam at the target is obtained with one achromat composed with two 4.5° bend. This allows for a cost reduction when compared to the previous design and an operation simplification. The achromat is located near the accelerating system output. At this location, the energy spread growth induced by the space charge is minimized. The line length after the deviation is set in order to reach the horizontal separation between the target center and the linac reference line. The present design is 5.3 m long, as shown in Figure 28, and this can be insufficient, but the lengthening of the last drift can increase this distance. The total line length is 43.12 m. Transverse uniform shape is obtained using non-linear multipole lenses (octupoles and duodecapoles).

The line is divided in three functional sections:

• The goal of the first section, which includes the achromat, is to match the linac output beam through the achromat and for the entry in the second section.

• In the second section, the optical conditions (see §6.5) are designed in order to allow for insertion of the octupole and duodecapole lenses at 4 positions.

• The last section, including the beam expansion drift, allows the matching of the needed footprint sizes at the target.

This organization allows an easy operation of the line tuning. All the first order simulations are performed with the code BETA [15].
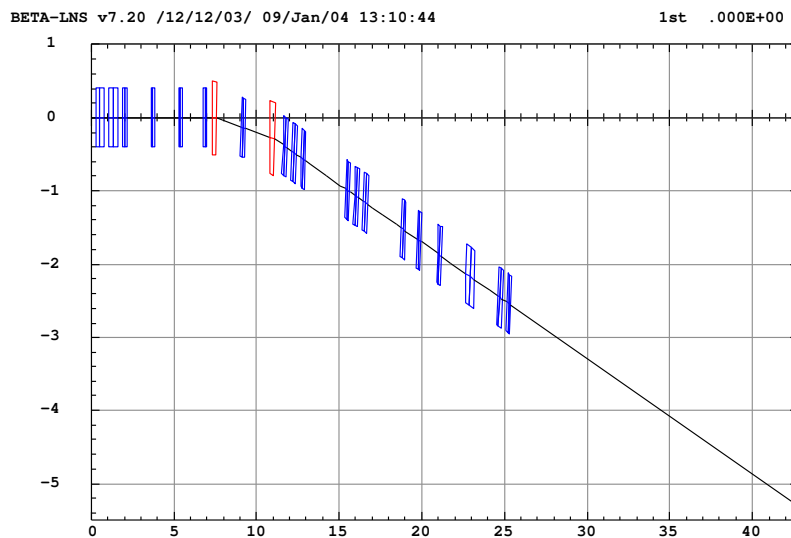
Figure 28: HEBT Layout.

6.4 Octupole tuning

The tuning of the octupoles [16,17] assume hypothesis. The transverse motions are supposed to be fully uncoupled (the space charge coupling is assumed negligible). The non-linear lenses dedicated to the horizontal distribution flatness (and respectively the vertical distribution) are supposed to be located at a waist of the vertical motion (respectively the horizontal). This allow to act on one plane with minimize effects on the other plane.

The beam ellipses in both the horizontal (x, x') and the vertical (z, z') phase spaces are supposed to be flat (if $\beta\gamma >> 1$, the ellipse is thin enough) at the non-linear lenses position. The beam at the octupolar lenses is described by its rms ellipse frontier:

$$\varepsilon_0 = \gamma_0 y_0^2 + 2\alpha_0 y_0 y_0' + \beta_0 y_0'^2 \quad \text{with } y = x, z$$

$\beta_0, \alpha_0, \gamma_0 = \dfrac{(1+\alpha_0^2)}{\beta_0}$ are the optical functions at the lenses and ε_0 is the rms emittance.

Let's write

$$y_0 = -\frac{\alpha_0}{\gamma_0} y_0' \pm \frac{1}{\gamma_0} \sqrt{\gamma_0 \varepsilon_0 - y_0'^2}$$

We consider the octupole case, the phase space coordinates at the target are:

$$\begin{pmatrix} y \\ y' \end{pmatrix} = \begin{pmatrix} T_{11} y_0 + T_{12}(y_0' + OL\, y_0'^3) \\ T_{21} y_0 + T_{22}(y_0' + OL\, y_0'^3) \end{pmatrix} \text{ where } OL \text{ is the octupole integrated strength } \left(OL = \frac{\mathbf{B}\, L}{a^3 B\rho} \right) \text{ with B}$$

the field at the pole-tip, a the radius at the pole-tip, L the octupole length and T_{11}, T_{12}, T_{21}, T_{22} are the terms of the 1st order transfer matrix between the octupolar lense and the target.

If the phase space ellipse is flat enough, one may consider that $y_0 \approx -\dfrac{\alpha_0}{\gamma_0} y_0'$, and by replacement in the previous equation this gives:

$$\begin{pmatrix} y \\ y' \end{pmatrix} = \begin{pmatrix} y_0'\left(\dfrac{-\alpha_0}{\gamma_0} T_{11} + T_{12}\right) - OL\, T_{12}\left(\dfrac{\alpha_0 y_0'}{\gamma_0}\right)^3 \\ y_0'\left(\dfrac{-\alpha_0}{\gamma_0} T_{21} + T_{22}\right) - OL\, T_{22}\left(\dfrac{\alpha_0 y_0'}{\gamma_0}\right)^3 \end{pmatrix}$$

The extent of the region of uniform density is comprising between $\pm y_M$, where y_M is defined as:

$$y_M = y_0'(y_M)\left(\frac{-\alpha_0}{\gamma_0} T_{11} + T_{12}\right) - OL\, T_{12}\left(\frac{\alpha_0 y_0'(y_M)}{\gamma_0}\right)^3 \text{ and } \frac{dy}{dy_0'}(y_0'(y_M)) = 0$$

By solving the equations:

$$y_0'(y_M) = \pm \frac{\sqrt{\dfrac{-\alpha_0}{\gamma_0} T_{11} + T_{12}}}{\sqrt{3\, OL\, T_{12}\left(\dfrac{\alpha_0}{\gamma_0}\right)^3}}$$

The particular value $y_0'(y_M)$ where the distortion occurs depends on the incoming probability density function f(y'$_0$). When f(y'$_0$) is gaussian with an rms value $\sigma_{y_0'} = \sqrt{\varepsilon_0 \gamma_0}$, it appears [14,15] that an optimum value is $y_0'(y_M) \approx \dfrac{4}{3}\sigma_{y_0'}$, this gives values for the octupole strength:

$$OL = \frac{3\left(\dfrac{-\alpha_0}{\gamma_0}T_{11}+T_{12}\right)}{16\left(\varepsilon_0\gamma_0 T_{12}\left(\dfrac{\alpha_0}{\gamma_0}\right)^3\right)},$$

and the uniform density beam extension:

$$y_M = \pm\frac{8}{9}\sqrt{\varepsilon_0\gamma_0}\left(\frac{-\alpha_0}{\gamma_0}T_{11}+T_{12}\right)$$

The two previous expressions depend on the optics between the octupole position and the target $\left(T_{11}=\sqrt{\dfrac{\beta_t}{\beta_0}}(Cos(\Delta\varphi)+\alpha_0 Sin(\Delta\varphi)), T_{12}=\sqrt{\beta_t\beta_0}Sin(\Delta\varphi)\right)$ (where β_t is the betatron function at the target and $\Delta\varphi$ the phase advance between the target and the octupole). All changes in the optics imply the change of the needed octupole strength. In the case of high intensity beam (i.e high space charge strength) the optic is modified. These expressions give the approximate octupole strength.

6.5 First order matching description

6.5.1 1st section, Linac to "Multipolar section" matching section:

Before being able to apply mutipolar lenses forces, one need a section to match the beam toward specific conditions. The quadrupole in-between the two bending magnets gives the achromatic conditions. The matching of the 6 following conditions is achieved with 6 quadrupoles:

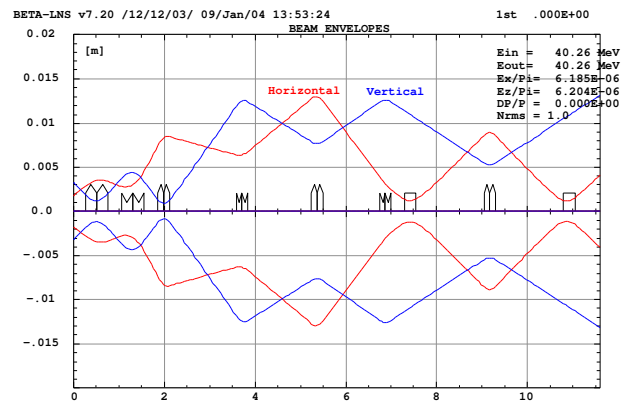o   2 symmetrical conditions (α_x=0, α_z=0) at the middle of the achromat,

Matching optical conditions (α_x, β_x, α_z, β_z) at the entry of the 2nd section.

The beam sizes, defined as $\sqrt{\beta_x\varepsilon_x+(D_x\delta)^2}$ in horizontal and $\sqrt{\beta_z\varepsilon_z}$ in vertical, are less than 1.5 cm, with ε_x=6.18 10^{-6} m.rad, ε_z=6.20 10^{-6} m.rad and δ=0 (see Figure 29 and Figure 30).
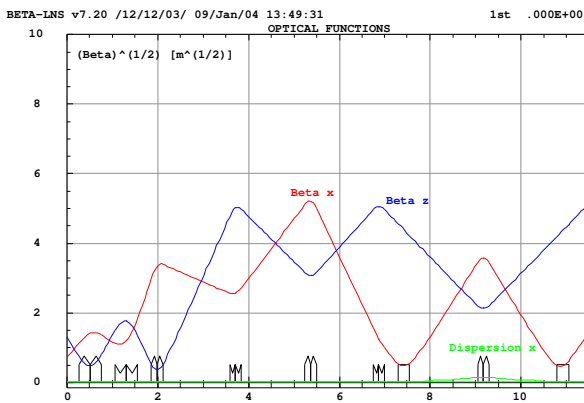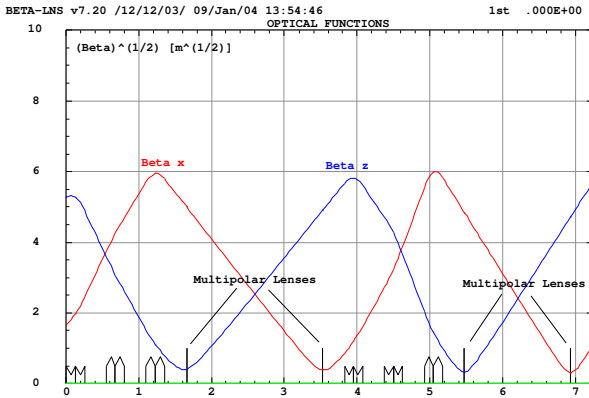

Figure 29: optical functions in the 1st section.

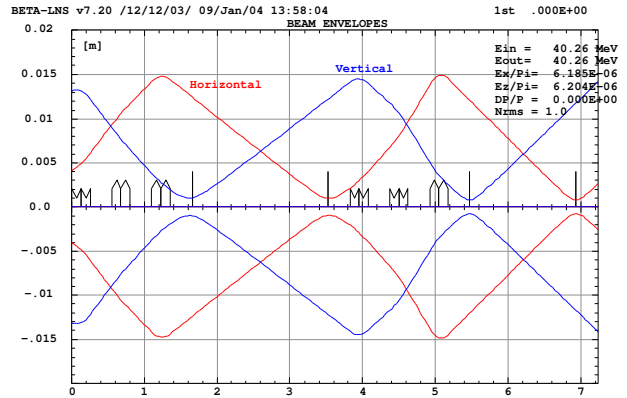Figure 30: beam envelopes in the 1st section.

6.5.2 2ⁿᵈ section, "Multipolar section":

Multipolar lenses (octupoles, duodecapoles) are used in order to obtain uniform beam density at the target. When the beam sizes, at the multipole location, are small in one plane and large in the other one, the multipole have an effect in the plane where the beam is sufficiently big. Four positions, where the beam sizes have the previous properties, are achieved with 6 quadrupoles. This allows for the insertion of 4 multipoles, 2 for each plane. In this section, like the previous section, the beam sizes are less than or equal to 1.5 cm (see Figure 31 and Figure 32).

Figure 31: optical functions in the 2nd section.

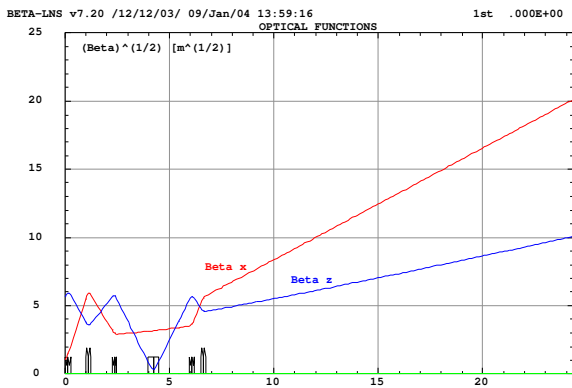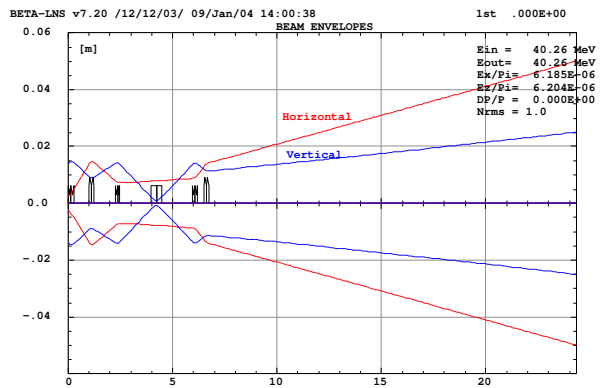Figure 32: beam envelopes in the 2nd section.

6.5.3 3ʳᵈ section, Footprint matching section:

The last section has to match the target footprint beam sizes to the requirements. This is made with 6 quadrupoles. Below are showed the full HEBT line optical functions for a 10×5 cm footprint beam size at the target. Figure 33 and Figure 34 show optical functions and beam envelopes of this section.
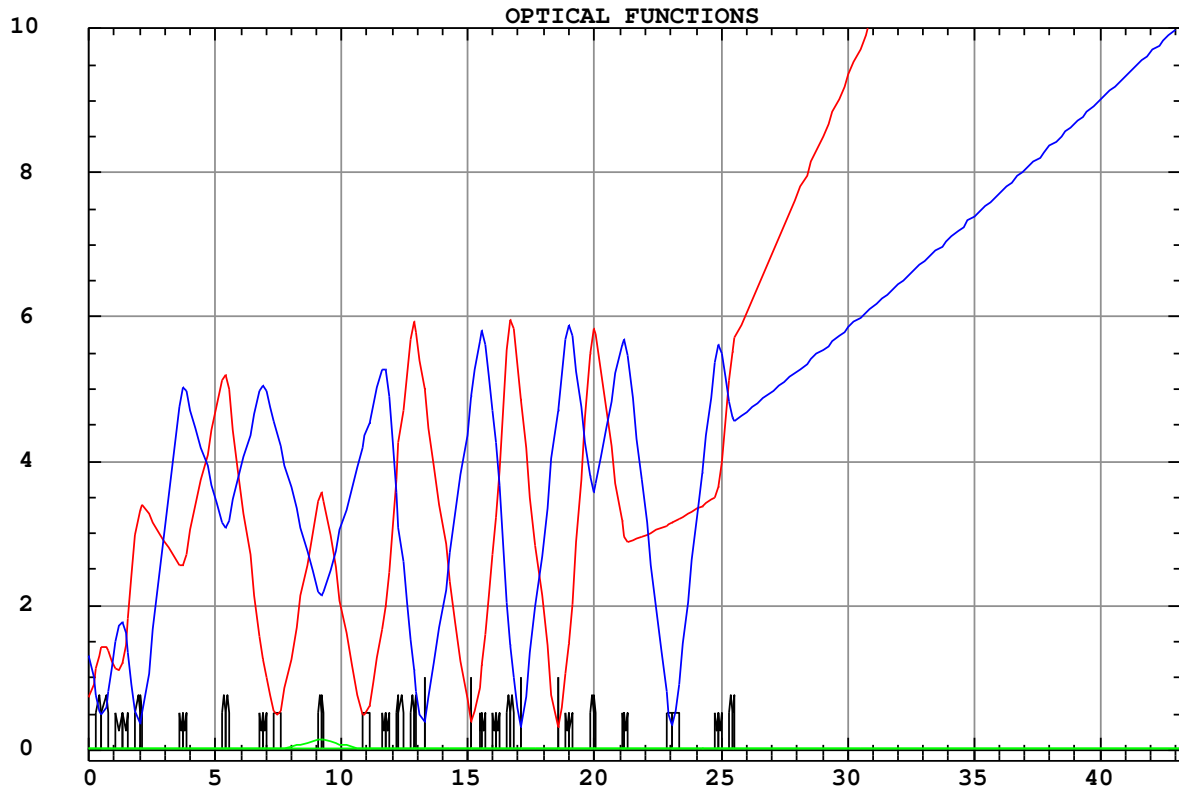

Figure 33: optical functions in the 3rd section.

Figure 34: beam envelopes in the 3rd section.

IFMIF HEBT v5.0.1c

Figure 35: full line optical functions.

6.6 PIC simulations

6.6.1 *Calculations framework.*

A 1,000,000 macroparticles 4D water-bag distribution is used at the input of the RFQ. The transverse rms normalised emittances used are $0.25\,\pi$.mm.mrad. The beam current is 130 mA. Multiparticle simulations are then done from the RFQ output in the full DTL. And finally, the output DTL beam distribution is injected in the HEBT line.

- Transport through the RFQs is done with TOUTATIS [11].

- Transport through the rest of the linac is done with TraceWin / PARTRAN [18] (with PICNIC [19] 3D space-charge routine, taken into account of the bunch overlap effect).

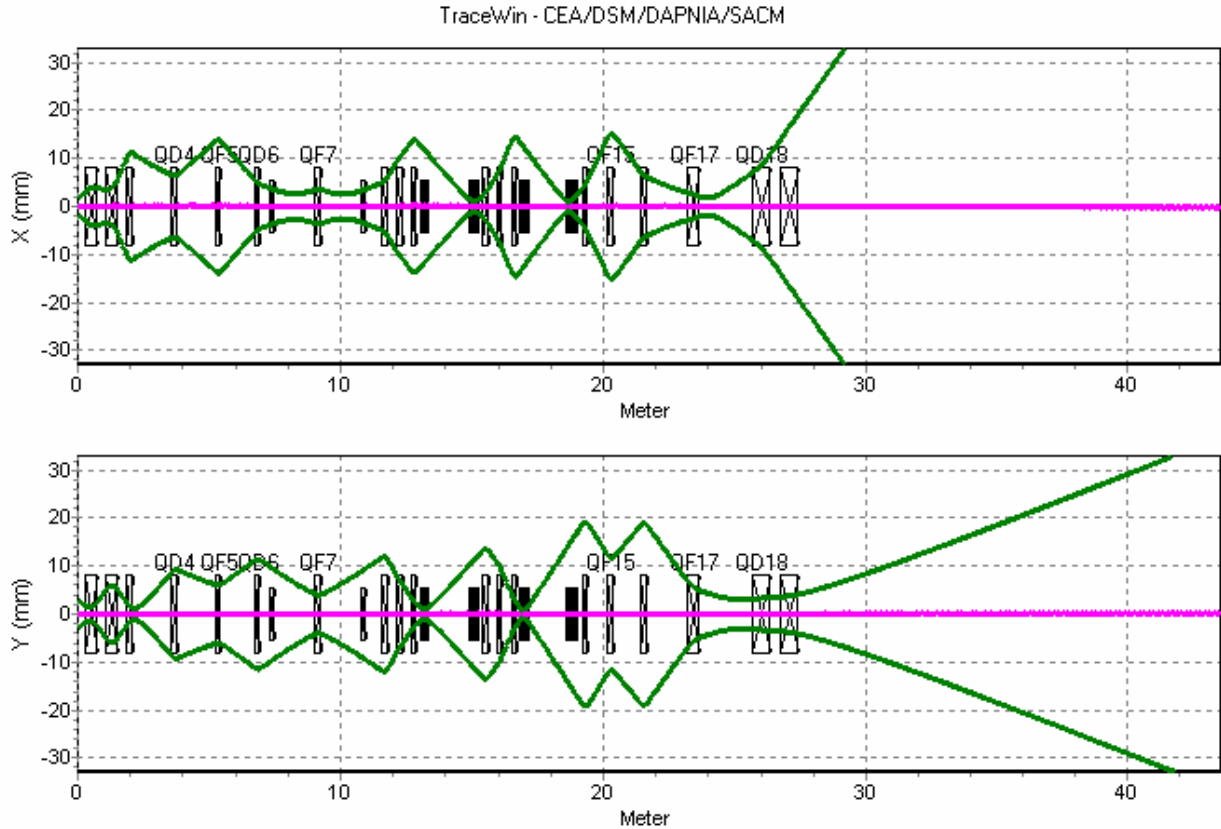The behaviour of the beam envelope in the HEBT is plotted below.

Figure 36: Transverse envelopes.

Due to the halo beam size (non linear effect such space-charge, non linear elements), we estimate than a beam pipe radius of 15 σ is necessary. Here, we use a beam pipe radius from 8 cm to 15 cm according to beam size. In the same time we have respected for the different magnetic elements a maximum field on the pole tip lower than 1 T. This implies an aperture lower than 5 cm for non linear lenses which is smaller than the required 15 σ. Indeed, to double the aperture in an octupole and duodecapole keeping the same strength, we have to multiply the field by 2^3 (8) and 2^5 (32) respectively. Two octupoles and two duodecapoles are used in order to reach the footprint requirement. The duodecapoles role is to improve the beam flatness by folding back the tails created by the octupoles. All the HEBT magnetic elements are listed in the following table.

Table 5. HEBT list of elements

Element	Length (mm)	Strength
QF1	500	6.9 T/m
QD2	500	-7.9 T/m
QF3	250	8.2 T/m
QD4	250	-5.3 T/m
QF5	250	4.5 T/m
QD6	250	-3.7 T/m
D1	3183	4.5 °
QF7	250	6.2 T/m
D2	3183	4.5 °
QD8	250	-6.1 T/m
QF9	250	1.1 T/m
QF10	250	5.2 T/m
DUO1	*400*	*0.25 T/m^5*
DUO2	*400*	*0.25 T/m^5*

QD11	250	-5.3 T/m
QD12	250	-2.9 T/m
QF13	250	7.8 T/m
OCT1	*400*	*-0.57 T/m^3*
OCT2	*400*	*0.98 T/m^3*
QD14	250	-4.6 T/m
QF15	250	6.6 T/m
QD16	250	-3.9 T/m
QF17	500	2.3 T/m
QD18	750	-0.74 T/m
QF19	750	0.04 T/m

6.6.2 Ouptut distribution

The output profile is illustrated by Figure 37 and Figure 38. These results indicate that the deviations from uniformity in the flat-top region are in the range of ± 7 %, rather than the desired ± 5 % in vertical plan (see Figure 39, Figure 40, Figure 41 and Figure 42) while the horizontal beam distribution fill up better than the requirements. The peaks along the horizontal edge rise are much better than the desired 15 %. But the 0.5 µA/cm² beam density beyond 22 cm are clearly out of reach, especially in a space-charge regime.
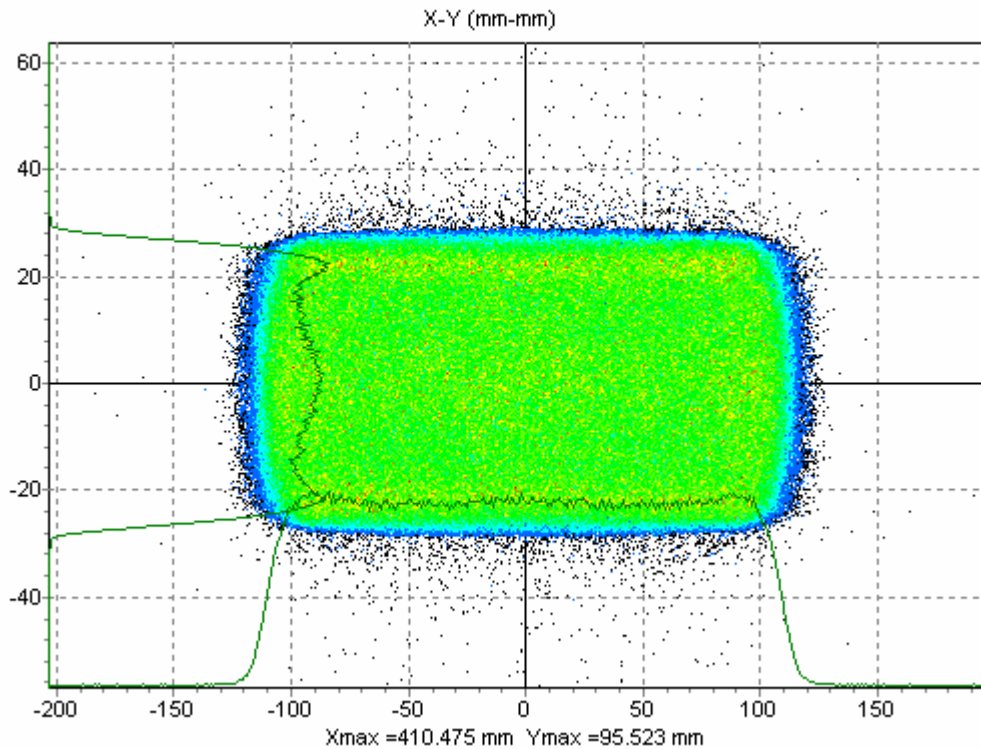

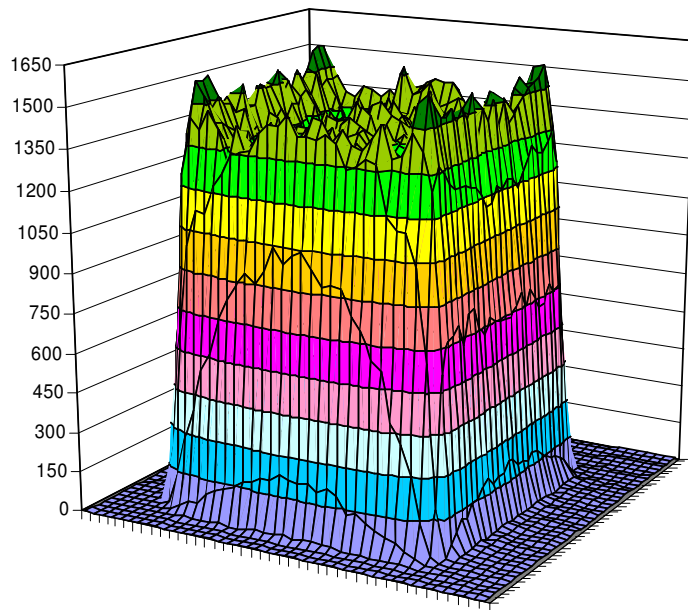Figure 37: Output HEBT beam distribution.

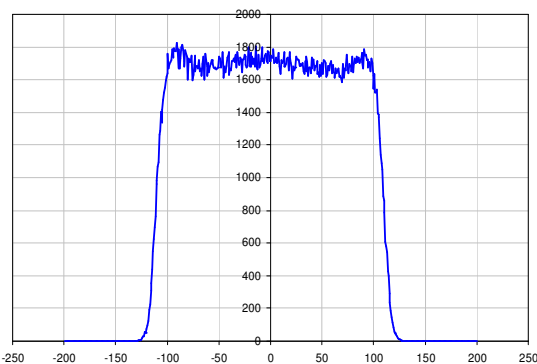Figure 38: 3D beam distribution at the target

Figure 39: Horizontal beam profile.
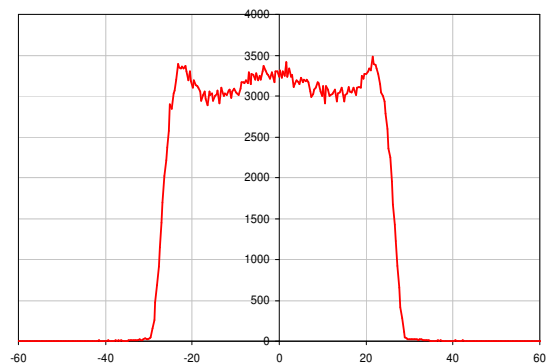

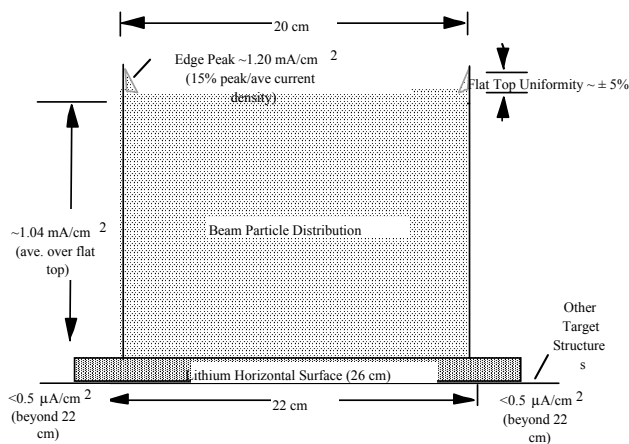Figure 40 : Vertical beam profile.

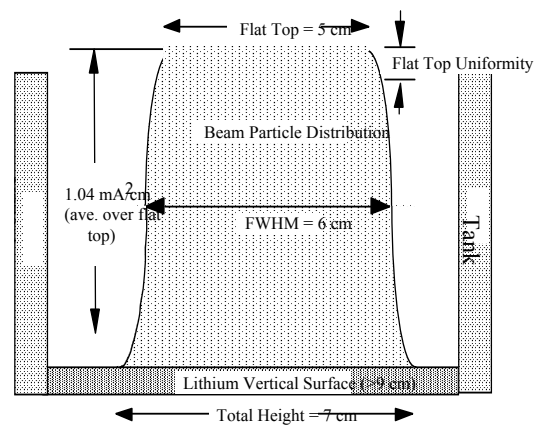Figure 41: Horizontal requirements

Figure 42: Vertical requirements

6.6.3   beam losses

The simulation using the beam distribution from the DTL shows losses mainly located in the non-linear lenses, where the pipe radius is the smallest (5 cm). About 44 macroparticles over 1,000,000 are lost. They correspond to about 6 μA and 240 W. The same simulation performed with an initial 4σ gaussian distribution shows no loss. For the same rms emittance, the total emittance from the DTL beam is 4 times bigger than the usual 4σ gaussian distribution (see Figure 43 and Figure 44) and 3 times bigger for the beam size. The Figure 45 shows the losses repartition in the HEBT.
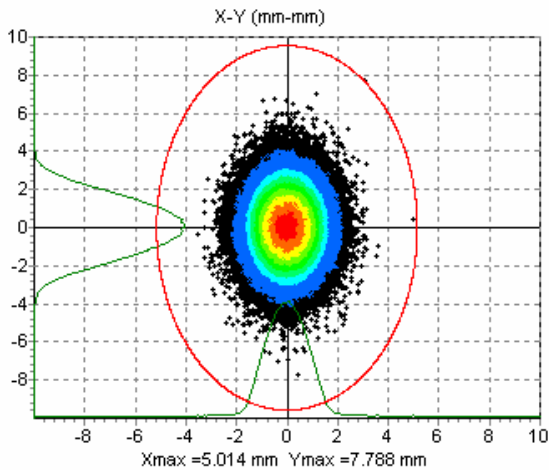
Figure 43: DTL output distribution.
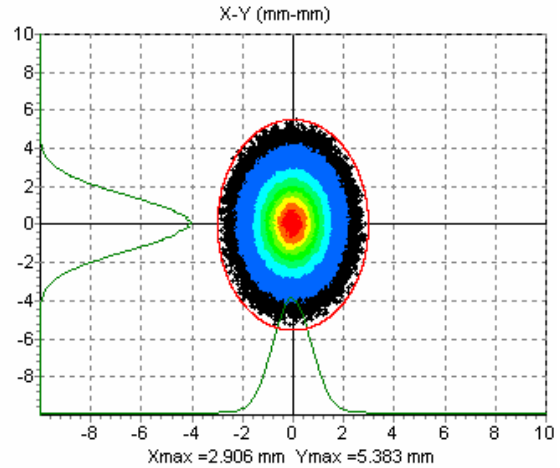
Figure 44: 4σ Gaussian.
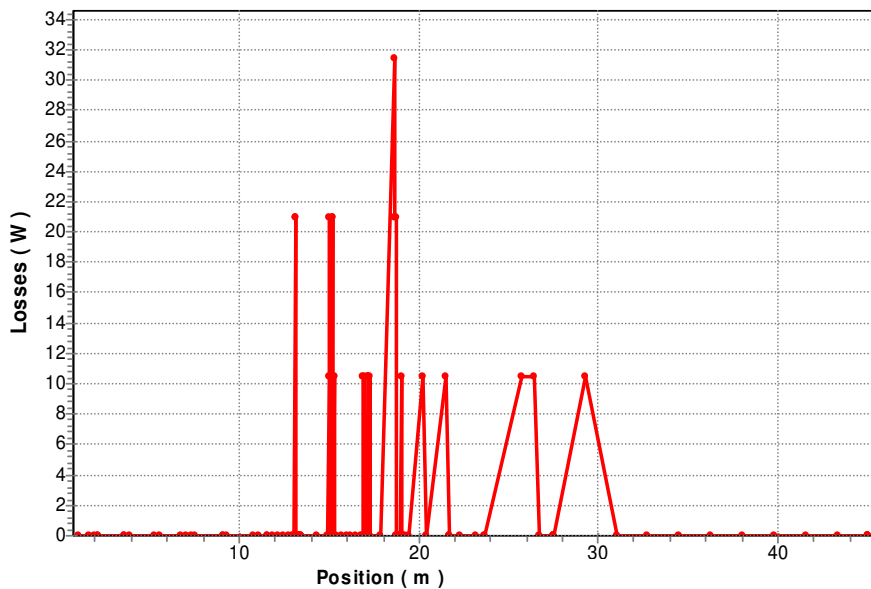
Figure 45: losses (W) along the HEBT.

A possible way to avoid losses all along the HEBT and minimize activation of the accelerator components is to reduce beam halo with a scraper. A dedicated scraper can be designed to support more easily the losses and allow easier shielding than multipole elements. The simulation shows no loss if it is located after the achromat line. The removed beam portion corresponds to 0.02 % (1 to 2 kW). The following graph (Figure 46) represents the different beam size radii and the aperture along the HEBT. The red line corresponds to 90 % of the beam, the blue one 99%, the green 99.9% …, the

black line includes the entire beam and the last black line represents the aperture. The scraper avoids the losses in the multipole lenses.

In this study, the 17 m drift between the last quadrupole and the target has an increasing aperture. This aperture should be lowered for practical reasons. As an example, if the maximum aperture is set to 200 mm (pink box), the lost beam fraction can easily be estimated by using these curves (Figure 46). Here, less than 1 particle over 10^6 will be lost.

Taking into account this point and the beam size, it appears that losses will mainly occur 23 m from the DTL end. At this location, just before the last doublet, a 2.3 m drift allows to insert a wall to separate the HEBT in 2 parts according to the radioprotection level.
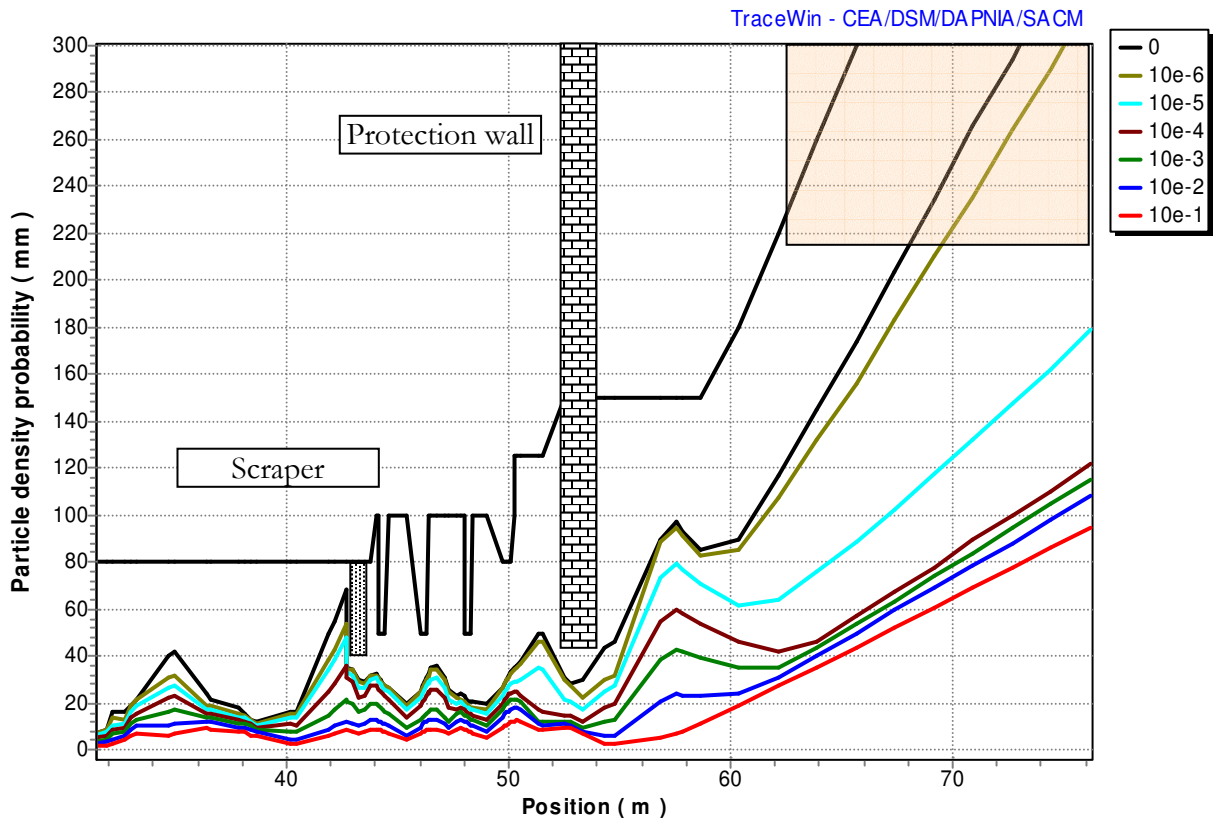
Figure 46: Beam size radii along the HEBT.

(10^{-1} corresponds to 90% of the beam, $10^{-2} \rightarrow 99\%$, $10^{-3} \rightarrow 99.9\%$ ...and le last black one: 100%)

6.7 Sensitivity to linac element errors

6.7.1 Introduction

In real life, the linac elements are a little bit different than expected. Quadrupoles may have a wrong position, be tilted, or have a wrong gradient. Cavities may have a wrong position, be tilted, or have a wrong field (phase and/or amplitude). An unperfect beam position measurement has also to be taken into account.

Two families of errors may occur:

- Static errors: the effect of these errors can be detected and cured with appropriate diagnostics and correctors. For example, beam position measurement coupled with steerers can compensate the

quadrupole or cavities misalignments. Correction strategy should be known to be able to estimate their impact on beam dynamics.

- Dynamics errors: the effect of these errors is assumed to be uncorrected. Fortunately, they have usually lower amplitude than static errors. There are, for example, the vibrations or the RF field variations (in phase or amplitude). They are responsible of orbit oscillations around the corrected orbit (this notion of orbit is also extended in the longitudinal motion).

The effect of the static errors depends on the orbit control system. A correction scheme has been studied. The positions of the beam position monitors and the associated steerers are described in the paragraph §6.7.2.

Errors with different amplitudes have been used depending on the linac section. The amplitudes of the errors are summarized bellow. For an error amplitude A, the element error has an equivalent probability to be between $-A$ and $+A$.

	Static	Dynamique
RFQ		
Machining transverse defect (mm)	±0.05	
Machining longitudinal defect (Z) (mm)	±0.05	
perpendicular tilt by segment (mm)	±0.1	
parallel tilt by segment (mm)	±0.1	
perpendicular displacement by segment (mm)	±0.1	
Parallel displacement by segment (mm)	±0.1	
MATCHING LINE RFQ-DTL		
Quadrupole gradient (%)	±0.5	±0.05
Quadrupole displacement (mm)	±0.1	±0.005
Quadrupole rotations (X,Y) (deg)	±0.15	±0.015
Quadrupole rotations (Z) (deg)	±0.25	±0.025
BMP accuracy (mm)	±0.1	
Cavity displacement (mm)	±0.1	±0.01
Cavity rotations (X,Y) (deg)	±0.05	±0.005
Cavity field phase (deg.)	±0.1	±0.01
Cavity field amplitude (%)	±0.1	±0.01
DTL		
Quadrupole gradient (%)	±0.5	±0.05
Quadrupole displacement (mm)	±0.1	±0.01
Quadrupole rotation (X,Y) (deg)	±0.15	±0.015
Quadrupole rotation (Z) (deg)	±0.25	±0.025
BMP accuracy (mm)	±0.1	
Cavity field phase (deg.)		±0.01
Cavity field amplitude (%)		±0.01
Tank displacement (mm)	±0.1	±0.01
[1]Tank rotations (X,Y) (deg)	±0.002	±0.0002
Tank field phase (deg.)	±1	±0.01
Tank field amplitude (%)	±1	±0.01

HEBT LINE		
Quadrupole gradient (%)	±0.5	±0.05
Quadrupole displacement (mm)	±0.1	±0.002
Quadrupole rotation (L=25 cm) (X,Y) (deg)	±0.03	±0.003
Quadrupole rotation (Z) (deg)	±0.25	±0.025
Multipole lens gradient (%)	±0.5	±0.05
Multipole lens displacement (mm)	±0.1	±0.02
Multipole lens rotation (X,Y) (deg)	±0.02	±0.002
Multipole lens rotation (Z) (deg)	±0.25	±0.025
BMP accuracy (mm)	±0.1	

The rotation angles (X,Y) have been calculated assuming an independent motion of element edges with amplitude defined in dx and dy. It corresponds to about $\arctan\left(\sqrt{2} \cdot \dfrac{dx}{Le}\right)$ with Le the element length.

There is no errors on the dipole elements in the present study.

6.7.2 Correction scheme

A correction-set is constituted of two steerers which kick the beam in both planes. They are associated with two Beam Position Monitors which measure in both planes the center. To correct beam misalignments in the DTL, such couple of steerers are placed into the last tubes of each tank and a couple of BPM are placed between tanks. In the HEBT, 6 correction-set are necessary to control efficiency the beam central trajectory. The correction scheme is efficient in the DTL (lower than 1 mm) and is more difficult in the HEBT line, especially in the last 17 m drift which is very sensible.

At present time, we did not include in our simulation specific diagnostics to correct the gradient errors which cause mainly mismatching. Thus, we consider that the error studies results below show a worse beam behavior that the normal operating mode where some specific diagnostics are used to match the beam to take into account the machine errors.

The rms value of the residual orbit along the DTL and HEBT is plotted on Figure 47. It is the result of a statistic over only 100 linacs. We notice that the rms jitter centroid position at the target is about 6 mm. It is due to the dynamics errors (vibrations: 5 μm for DTL, 2 μm for HEBT). In order to reduce the jitter, vibration tolerances have to be significantly lowered. We should notice that they are already challenging.
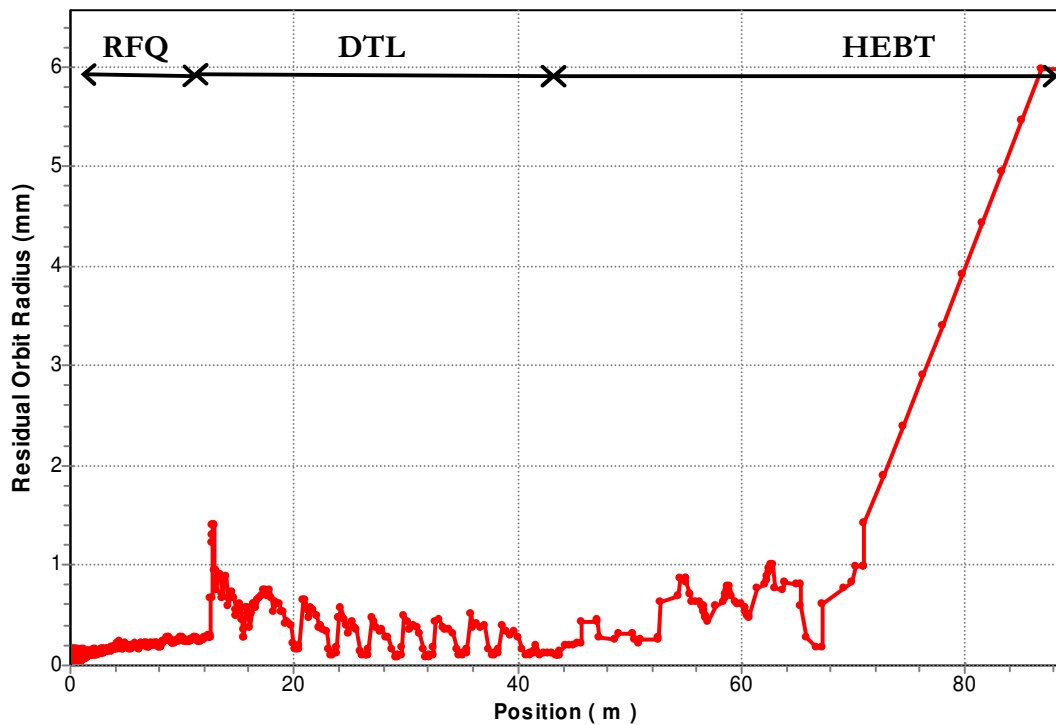
Figure 47: Residual orbit RMS value along the linac.

6.7.3 *Error studies*

6.7.3.1 **HEBT line**

We studied first the HEBT line alone. The transport of a 100,000 macroparticles beam has been simulated in a set of 110 different HEBT lines with all combined errors on each element. The total number of particles used is about 10 millions. The beam distribution from DTL has been used. The Figure 48 shows the statistical distribution of the particles along the HEBT. The red line corresponds to 90 % of the beam; the blue one 99%..., the black line includes the entire beam and the last black line represents the aperture. We observe that 1200 W are dissipated in the scraper. For a pipe radius limited at 200 mm, 1 particle over 10^6 will be lost.
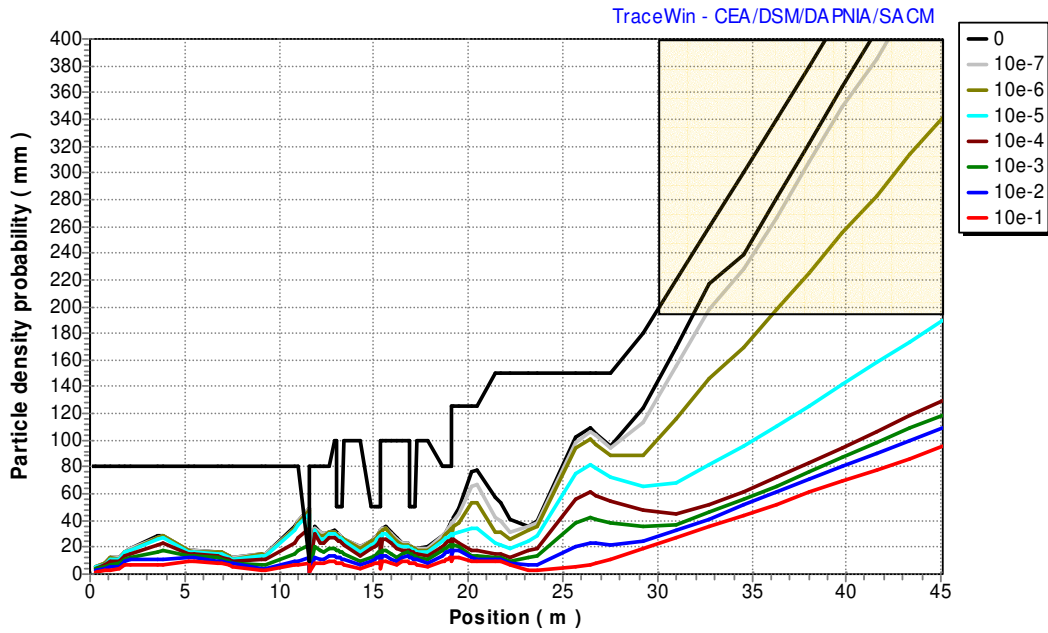
Figure 48: Beam size radii along the HEBT.
(10^{-1} corresponds to 90% of the beam, $10^{-2} \rightarrow 99\%$, $10^{-3} \rightarrow 99.9\%$ ...and le last black one: 100%)

The distribution in Figure 49 represents the superposition of 100 different simulated linacs with all the combined errors (about 10,000,000 particles). It's not the beam at the target, but the probability to reach this density at the target. We notice that the distribution is still close to the requirements. The imperfections mainly degrade the **beam fringes and increase the beam noise**.
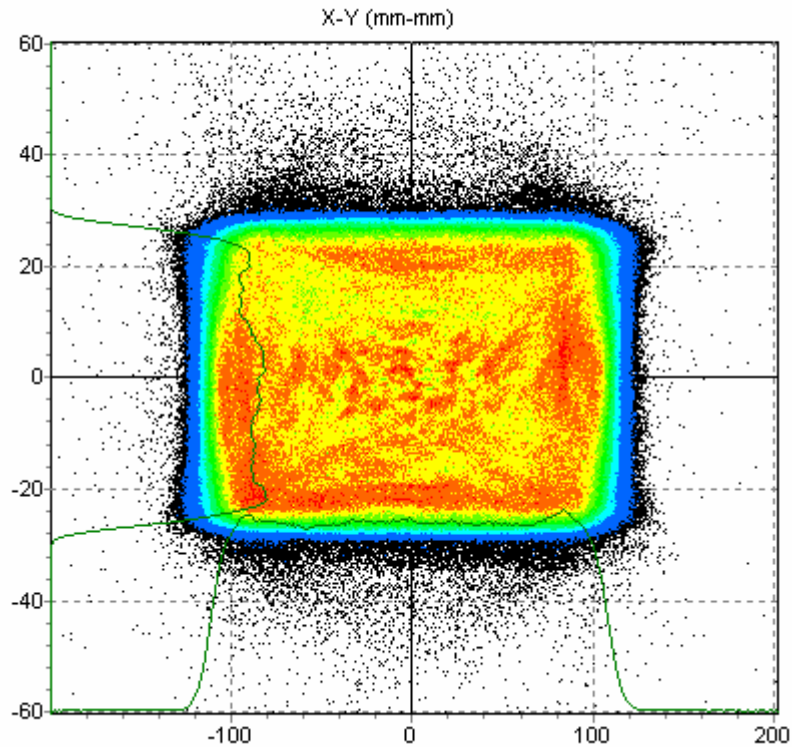

Figure 49: Output HEBT beam distribution (HEBT error).

6.7.3.2   *End-to-End errors study*

The linac (RFQ-DTL) used in this study is the IFMIF reference design [20]. The transport of a 100,000 macroparticles beam has been simulated in a set of 110 different linacs with all combined errors on each element. The total number of particles used is about 10 millions. The simulation begins at the RFQ input. All the previously listed errors are used. Figure 50 shows the envelope behavior along the IFMIF design without error. Figure 51 and Figure 52 represent the different beam size radii along the RFQ, DTL and HEBT (The overall figure is separated in 2 for visibility reasons). Figure 53 shows the beam distribution at the target taking into account all the errors. It has to be repeated that all these results include mismatching errors without any correction. The output distribution characteristics are close to the requirement expected 0.5 µA/cm² beam density beyond 22 cm.
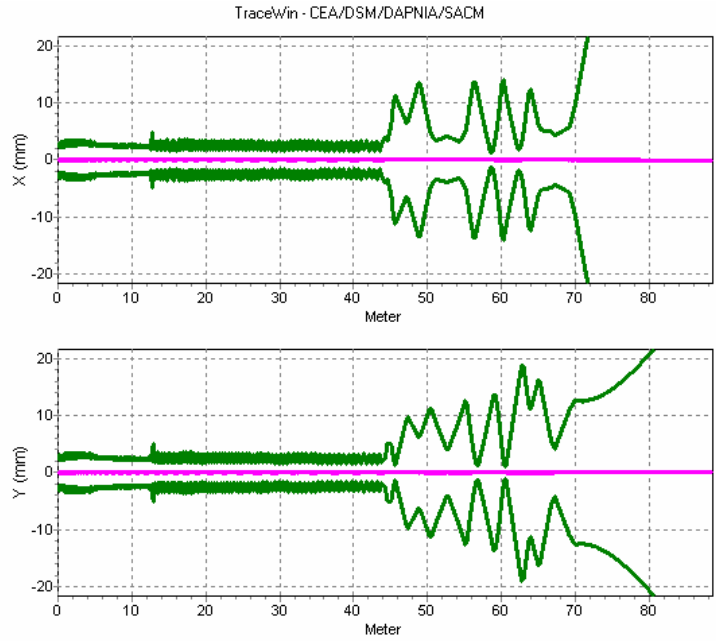

Figure 50: Transverse envelopes (RFQ-DTL-HEBT).
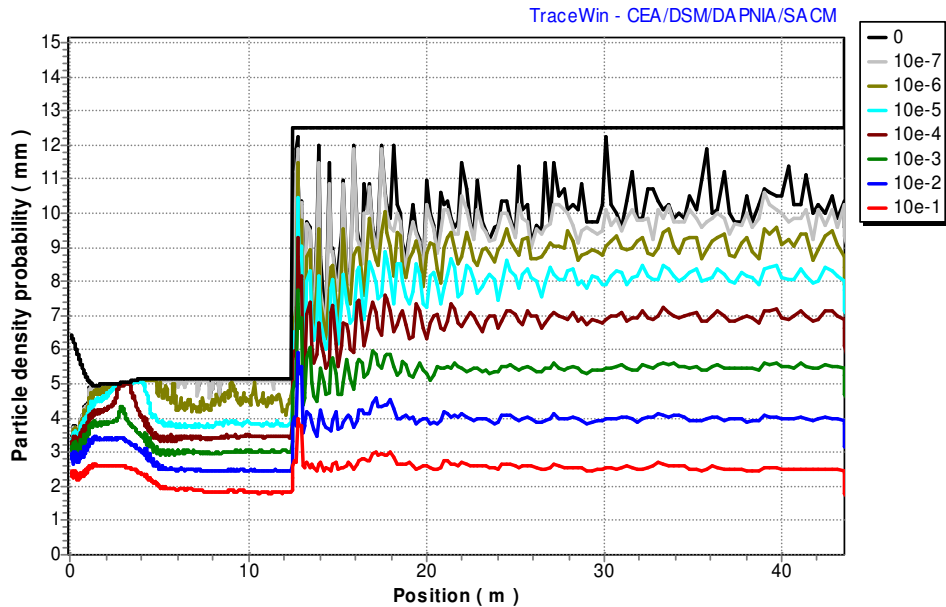
Figure 51: Beam size radii along the RFQ and DTL.
(10^{-1} corresponds to 90% of the beam, $10^{-2} \rightarrow 99\%$, $10^{-3} \rightarrow 99.9\%$ ...and le last black one: 100%)
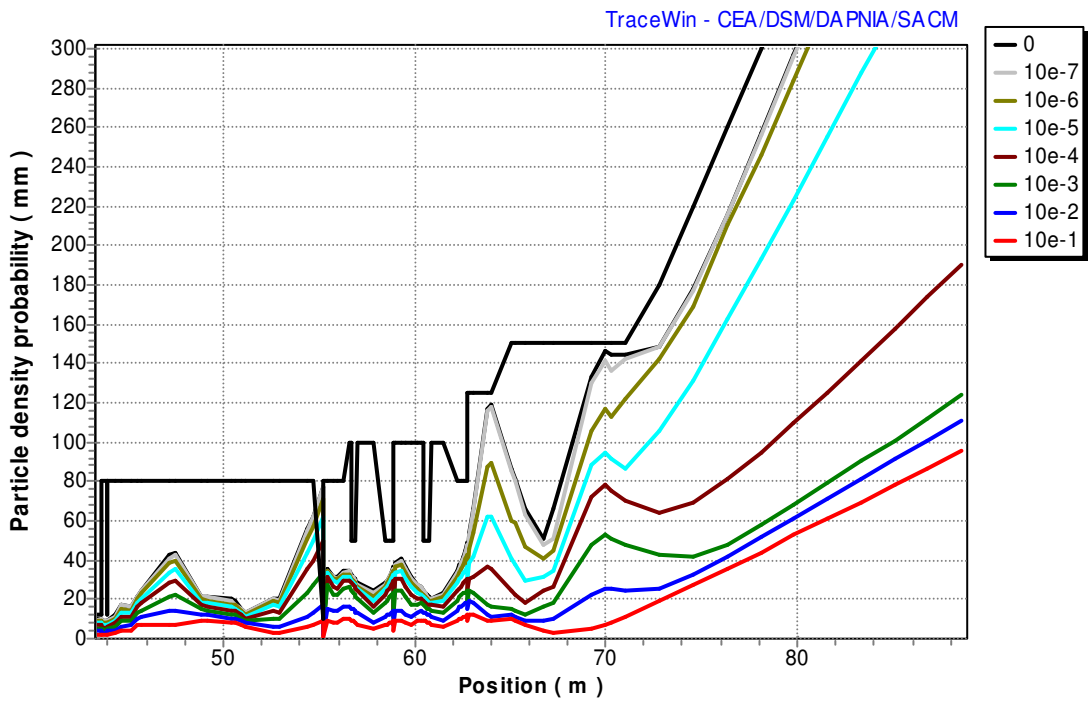
Figure 52: Beam size radii along the HEBT.
(10^{-1} corresponds to 90% of the beam, $10^{-2} \rightarrow 99\%$, $10^{-3} \rightarrow 99.9\%$ ...and le last black one: 100%)
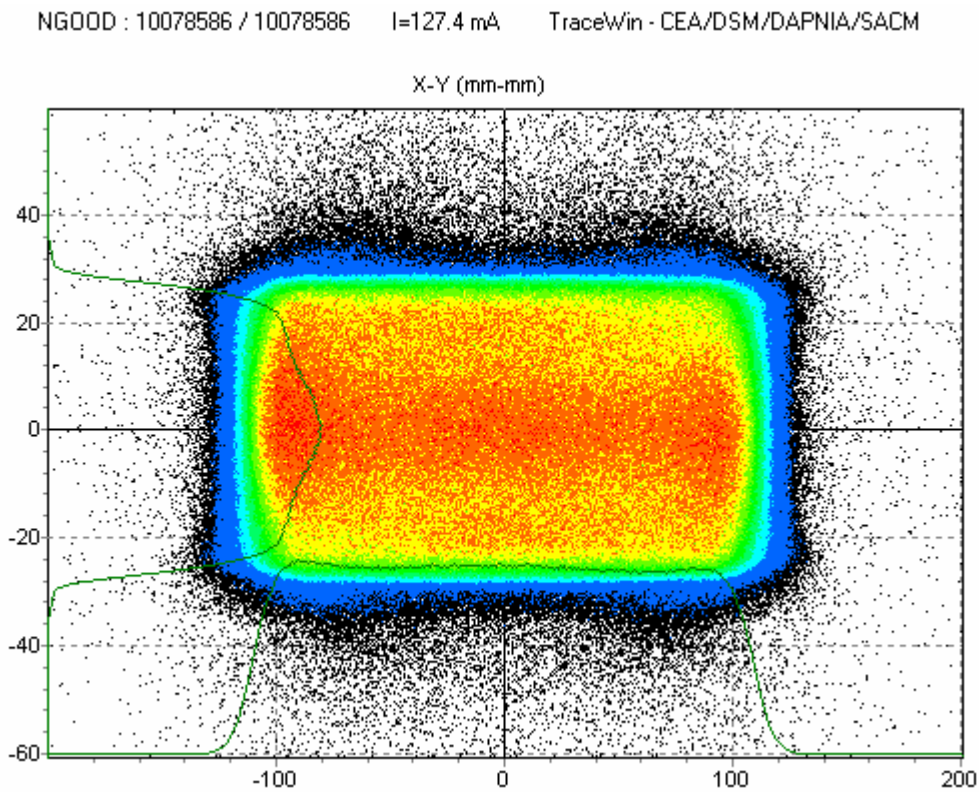

Figure 53: Output HEBT beam distribution (Full linac error)

Figure 54 gives the losses repartition along the structure and the corresponding dissipated power. This repartition is 1.98 % in the RFQ, 0.18 % in the DTL and 0.17 % in the HEBT. Remember that no matching has been used to control the beam mismatching due to focalization errors, while it will be partially corrected in real operation.

The first end-to-end errors study made in 2002 didn't show any loss in the DTL [20]. Two reasons explain the today results:

- More errors have been taken into account like vibrations, phase and field errors, tanks displacements and vibrations, BPM errors…

- The statistic was 100 runs of 10,000 macro particles compared to the 100 runs of 100,000 macro particles of the present study. It didn't allow to observe loss intensity lower than 128 nA.
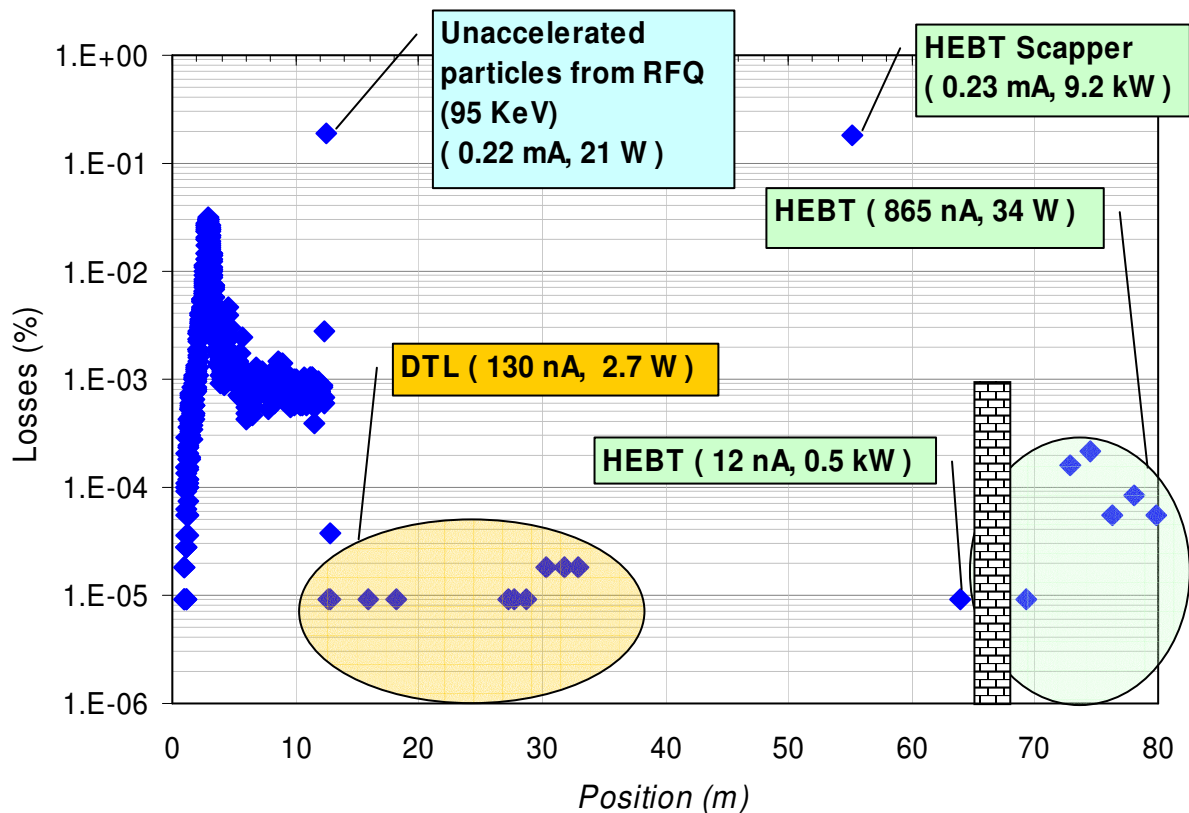
Figure 54: Losses repartition along the structure.

Several methods can be explored in order to reduce these losses:

- change the DTL design without increasing the number of diacrode, in order to increase the aperture drift tube from 12.5 mm to 14 mm or more (see following section),

- the RFQ machining tolerance could be slightly decreased.

Concerning the HEBT losses, the extra dissipated power in the scraper compared to the nominal case (1 kW) comes from the beam mismatching. In normal operating mode the beam will have to be match in order to control this power. Moreover, this scraper could be an interesting diagnostics to manage that.

6.7.4 Alternate DTL design

The main losses in the DTL are located after the 4th tank. They easily can be avoided by using 2 different quadrupole lengths rather than only one along the DTL (present design). Using a longer quadrupole for the longer drift tubes allows increasing the inner drift tube radius without necessary increasing the outer drift tube and the RF power.

Another method is simply to scale all the drift tube and quadrupole dimensions like described below. The aperture may then be increased without an enhancement of the maximum field on the pole field tip.

Drift tube aperture	**: 1.25 cm**	**→ 1.4 cm**
Drift tube radius	: 9.6 cm	→ 9.75 cm
Quadrupole length	: 7.8 cm	→ 8.6 cm
Quadrupole radius	: 7.6 cm	→ 7.75 cm

Thus, no extra power will be asked for the quadrupole power supply. The copper drift tube surface is slightly increased, but, in the reference design, only one third of the available power is used in the last tank. So, a new DTL designs has been generated with the GENDTL code [21] and the results are summarized below. The conclusion brings that it is possible to increase the aperture.

Table 6 : Main and new DTL characteristics

	Reference	**1.4 cm**
Number of diacrode	10	10
Number of cells	119	121
Total power (Pt)	6.34 MW	6.46 MW
Power dissipation	1.86 MW	1.98 MW
Beam power (Pb)	4.48 MW	4.48 MW
Efficiency (Pb / Pt)	71 %	69 %

The Figure 55 corresponds to the beam repartition in the DTL according to the radius. An extrapolation can give an idea on the losses for bigger DTL aperture.
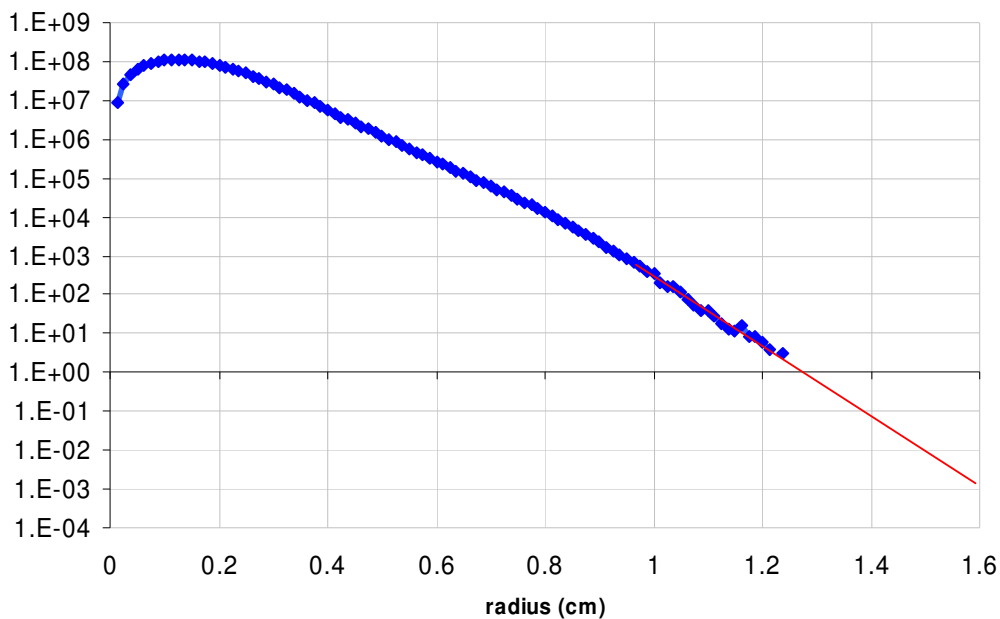

Figure 55: Particles repartition along the DTL (red line is the extrapolated curve).

6.8 Conclusion

We demonstrated the existence of a HEBT design solution.

The end-to-end studies show manageable losses if we accept localized scrapers (localised losses, easier shielding and protection of multipole elements). The reduction of losses in the HEBT line can be achieved. Increasing the multipole lens aperture will allows to reduce the beam part dissipated on the scraper and may allow to remove it. A specific study should have to be lead on this issue.

We managed some room for insertion of radioprotection walls against the losses at the end of the 17m long drift tube.

The amplification of this 17m long last drift implies very strict dynamics tolerances on the previous elements. On this design, the value is challenging but exists in other machine like the photon machines.

Some works are still possible to improve the design, like a DTL optimised in terms of aperture.

All the beam characteristics requirements at the target can be reached using multipole lenses, excepted for the horizontal edges (0.5 μA/cm² beam density beyond 22 cm).

7 Conclusion

The tasks were completed on time, with extremely valuable results. The main points are:

- A dedicated H_2^+ has to be developed if the idea of using H_2^+ is kept for the linac conditioning.

- The RFQ 2D profile optimization lead to a diacrode saving. Only 2 1 MW diacrodes are now needed.

- The HEBT has been designed and extensively analysed. The requirements cannot be completely obtained on some points, due to the space charge. A full errors study was made, that we can describe as the "worse case". It appears that a scraper is highly recommended in the HEBT line. Some room was left for a wall shielding.

8 Contacts and Author list

Main contact people:

Pierre-Yves Beauvais : pybeauvais@cea.fr	IPHI project leader
Raphael Gobin : rjgobin@cea.fr	ECR source
Patrick Ausset : ausset@ipno.in2p3.fr	Diagnostics
Romual Duperrier : rduperrier@cea.fr	Beam dynamics
Didier Uriot : duriot@cea.fr	Beam dynamics
Jacques Payet : jpayet@cea.fr	Beam dynamics
François Simoens : fsimoens@cea.fr	RFQ tuning
Alain France : afrance@cea.fr	RFQ tuning
Aline Curtoni : acurtoni@cea.fr	2D RFQ optimisation
Pierre-Emmanuel Bernaudin : pebernaudin@cea.fr	DTL hot model

Task leader :

Robin FERDINAND

DSM/DAPNIA/SACM

CEA-Saclay

Tél: +33 (0) 1 69 08 96 91

Fax: +33 (0) 1 69 08 14 30

e-mail: rferdinand@cea.fr

9 References

[1] P-Y. Beauvais, "Status report on the construction of the French high intensity proton injector (IPHI)", proceeding of EPAC 2002, Paris, page 539-541

[2] R. Gobin et al., "High intensity ECR ion source (H+, D+, H-) developments at CEA Saclay", ISIS2001 conference, RSI, Vol.73, n°2, February 2002 (922)

[3] CEA-DSM-DAPNIA-SACM contribution to the IFMIF KEP phase June 2000 to December 2002, Ref DSM/DAPNIA 03-72:

[4] "Power consumption comparison between different RFQ structures in favour of the RIA project", Romuald Duperrier CEA-Saclay, Felix Marti NSCL, MSU note, November 2002, 12 pages.

[5] H. Podlech et al., "Electromagnetic design of an 80.5 MHz RFQ for the RIA driver linac", proceeding of the EPAC 2002, Paris, France, p. 942.

[6] W. D. Cornelius, "CW Operation of the FMIT RFQ Accelerator", p 3139, Proc. of the 1985 Particle Accelerator Conf.

[7] L. Young, "Segmented Resonant Coupled RFQ", proceeding PAC 1993, Washington, D.C..

[8] H. V. Smith Jr, J. D. Schneider and R. Sheffield, "Low-Energy Demonstration Accelerator (LEDA) Test Results and Plans", proceeding of PAC 2001, Chicago, page 3296-3298

[9] P.-Y. Beauvais et al., "Status report on the Saclay High Intensity proton injector project (IPHI)", proceeding of EPAC 2000, p. 283.

[10] J. D. Schneider, "A review of high beam current RFQ accelerator and Funnels", p.128, Proc. of the EPAC'98 Conference

[11] Romuald Duperrier thesis, "Dynamique de faisceaux intenses dans les RFQs", université Paris sud Orsay, n° 6194, july 2000. Exist in English version.

[12] A. Pisent et al., "Equivalent lumped circuit study for the field stabilization of a long four-vanes RFQ", Linac98

[13] J.H. Billen, "RFQ design codes"

[14] JAERI-Tech 2003-005, IFMIF-KEP, Key element technology phase report.

[15] J. Payet. BETA code

[16] F. Meot, T. Aniel, Principles of the non-linear tuning of beam expander NIM A379 (1996)

[17] F. Meot, T. Aniel, On beam uniformization by non-linear optics CEA/DSM/GECA/ 95-05, July 1995

[18] R. Duperrier, N. Pichoff, D. Uriot, "CEA Saclay codes review", ICCS confererence, Amsterdam, 2002.

[19] N. Pichoff, J. M. Lagniel, and S. Nath, "Simulation Results with an Alternate 3D Space Charge Routine, PICNIC," Proceedings of the XIX International Linac Conference, p 141, Chicago.

[20] R. Duperrier, D. Uriot , N. Pichoff , R. Ferdinand "Beams dynamics end to end simulations in IFMIF Linac" EPAC 2002, Paris.

[21] D. Uriot, N. Pichoff, "GENDTL", internal report CEA/DSM/DAPNIA/SEA/2000/46